

Bachelor's thesis

**Properties of Supersymmetric
Top Quark Pair-Production
at Hadron Colliders**

Simon May

30th September, 2015

Advisor: Jun.-Prof. Dr. Anna Kulesza
Institut für Theoretische Physik
Westfälische Wilhelms-Universität Münster

Contents

1. Introduction	3
2. Elements of quantum field theories, the Standard Model and SUSY	6
2.1. The Standard Model of particle physics	6
2.2. Supersymmetry and the Minimal Supersymmetric Standard Model .	8
2.3. Experimental searches and exclusion limits	11
2.4. Feynman diagrams and Feynman rules	12
2.4.1. Canonical quantization and the S matrix	13
2.4.2. The path to Feynman diagrams	16
2.5. SUSY-QCD Feynman rules	19
3. Stop quark pair-production	22
3.1. Stop quark production at leading order	23
3.1.1. Production processes and matrix elements	25
3.1.2. Partonic cross sections	27
3.1.3. Hadronic cross sections	29
3.2. Next-to-leading order	30
4. Numerical analysis and results	31
4.1. Leading order	31
4.2. Scan of the parameter space at next-to-leading order	33
4.2.1. Approach	33
4.2.2. Results	35
5. Conclusion	43
A. Notation and conventions	45
B. Technical details	47
Bibliography	48

1. Introduction

“[...] the grand underlying principles have been firmly established. [...] further truths of physics are to be looked for in the sixth place of decimals.”

(Albert A. Michelson in 1894 [Fla92])

The *Standard Model of particle physics* (SM) provides a very accurate description of high-energy processes at the smallest scales and its predictions have been tested time and again in a multitude of large-scale experiments. At particle accelerators like the *Large Hadron Collider* (LHC), massive amounts of data have been generated and yet, no clear deviation from the Standard Model has been found. Indeed, with the discovery of the Higgs boson¹ in 2012, another long-predicted part of its theoretical framework was confirmed. However, being not so complacent (or cynical, depending on one's outlook) as Michelson in 1894, it is clear today that the established models and theories must be incomplete. In fact, a large goal of the LHC and the research around it is to discover “new physics” not yet explained by standard theories – for some, this even goes as far as showing hints of disappointment when the discovered Higgs boson did exhibit some of those properties which were predicted by theory. With the LHC's second round of operation in early 2015 with a collision energy of $\sqrt{s} = 13$ TeV (to be increased to 14 TeV in the near future), it will continue its mission to uncover “physics beyond the Standard Model” at high energy scales.

The subject of this thesis is part of this great unknown potentially dwelling in the regions that will be probed by the LHC. For as much as an achievement the Standard Model is, it is unable to provide explanations for some important phenomena. Setting aside that it (and the whole of quantum physics) does not account for gravity, one of the four fundamental forces, it does not, for example, provide a viable candidate for dark matter, which seems to make up a much larger portion of the matter content of the universe than the known “ordinary” matter. *Supersymmetry* (SUSY) provides a natural extension of the Standard Model by adding an additional boson-fermion

¹or at least a “Higgs-like particle”

symmetry. In the *Minimal Supersymmetric Standard Model* (MSSM), every known elementary particle gains a supersymmetric “twin” or *superpartner* with identical properties except for spin (differing by $1/2$) and mass (due to symmetry breaking); thus, for Standard Model bosons, these partners are fermions, while for fermions, the superpartners are bosons [Mar11, ch. 1]. If some version of supersymmetry were confirmed to be physical reality, it would provide a plausible dark matter candidate in the form of the *lightest supersymmetric particle* (LSP). SUSY can also more easily be combined with General Relativity to form a theory of *supergravity* (SUGRA). More indications are provided by the so-called “weak-scale instability problem” or “hierarchy problem”, to which SUSY is one possible solution – but only if the masses of SUSY particles are approximately degenerate and not much larger than the TeV scale –, the lack of gauge coupling unification in the Standard Model (which can be achieved in the MSSM) and the more natural explanation of electroweak symmetry breaking which is possible with SUSY [Ait05, section 1]. Due to the lack of evidence for supersymmetry in the first run of the LHC (2010–2013, $\sqrt{S} = 7$ TeV and 8 TeV), some have even raised concerns about a “crisis” in physics, as discarding supersymmetry would leave many of the questions mentioned above unanswered without a clear theoretical candidate to resolve them.

This work scrutinizes a specific supersymmetric process predicted to be very relevant to hadron colliders like the LHC. The total cross sections for the pair-production of the lightest supersymmetric top quarks (stop quarks, $\tilde{t}_1 \bar{\tilde{t}}_1$) in proton-proton collider experiments are calculated numerically. The MSSM, even more so than the Standard Model, suffers from a large number of parameters (exceeding 100 [Hab98]) unable to be derived from the theory. Exacerbating the problem, the Standard Model parameters can be obtained by experimentation, while it is not yet clear if supersymmetry is a description of physical reality at all. As such, calculation of the cross sections is only possible using assumed values for the parameters (such as the light stop mass $m_{\tilde{t}_1}$).

To obtain useful predictions for experimental data, however, it is necessary to have some information about how different values for the relevant parameters can affect the resulting cross section. Thus, the variation of the cross section of stop quark pair-production with its parameters is examined in leading order (LO) and next-to-leading order (NLO). The masses of the “lighter” squark flavors (other than stop) are assumed to be degenerate. For the given process, this results in a parameter space of five unknown parameters, namely the stop masses $m_{\tilde{t}_1}$ and $m_{\tilde{t}_2}$, the degenerate squark mass $m_{\tilde{q}}$, the gluino mass $m_{\tilde{g}}$ and the mixing angle, usually given as $\sin(2\theta_{\tilde{t}})$.

Scanning the parameter space, the effect of varying parameters on the cross section is studied and intervals of the values taken by the cross section as the parameters are varied are provided. Using this information, the maximum error on the cross section made by assuming certain values for the parameters can be estimated.

In chapter 2, basic elements of the current scientific understanding of particle physics due to the Standard Model are outlined. Supersymmetry is presented as a possible theoretical extension of this already-accepted knowledge and motivation is provided to illustrate why it is proposed as a strong candidate for physics beyond the Standard Model. Moreover, Feynman diagrams are introduced as the standard way to calculate cross sections in scattering experiments. Continuing to chapter 3, the method of Feynman diagrams is applied to the specific process considered in this work: the production of stop-antistop pairs at hadron colliders. For this, scattering of individual quarks and gluons has to be considered first before proceeding to hadronic scattering. In chapter 4, the numerical results obtained by the computer code developed for this work and by the established program Prospino [BHS96] are presented. Finally, the results are discussed and summarized in chapter 5. Refer to appendix A for remarks on conventions and notation.

2. Elements of quantum field theories, the Standard Model and SUSY

In this chapter, some basic properties of the Standard Model and of SUSY are presented. Moreover, *Feynman diagrams* are introduced as a method to calculate cross sections of scattering processes and their derivation from quantum field theory is sketched. The *Feynman rules* necessary for the calculations of cross sections are given in section 2.5.

2.1. The Standard Model of particle physics

As mentioned above, the Standard Model of particle physics provides an accurate description of three of the fundamental interactions (electromagnetic, strong and weak) and has been thoroughly tested up to the TeV scale. The fundamental particles of the Standard Model and their interactions are illustrated in fig. 2.1. The Standard Model fermions are divided into two groups called *quarks* and *leptons*, where quarks take part in the strong interaction while leptons do not. Composite particles made up from three (valence) quarks are called *baryons*, while those consisting of a quark-antiquark pair are referred to as *mesons*. All SM fermions and the weak gauge bosons take part in the weak interaction and all charged particles participate in the electromagnetic interaction. The four spin-1 gauge bosons mediate the forces between the different particles. The scalar Higgs boson stems from the Higgs mechanism which is responsible for endowing the particles with mass.

The strong interaction is very important for processes at the nuclear and sub-nuclear scale. It is described theoretically by *quantum chromodynamics* (QCD). As shown in fig. 2.1, quarks and gluons are the particles which participate in the strong interaction and so are part of QCD. As its name suggests, the strong interaction is the strongest of the fundamental interactions, but it is only effective at very small length (or very high energy) scales. In fact, it is so strong that quarks or gluons can never directly be observed individually as free particles and only be studied through

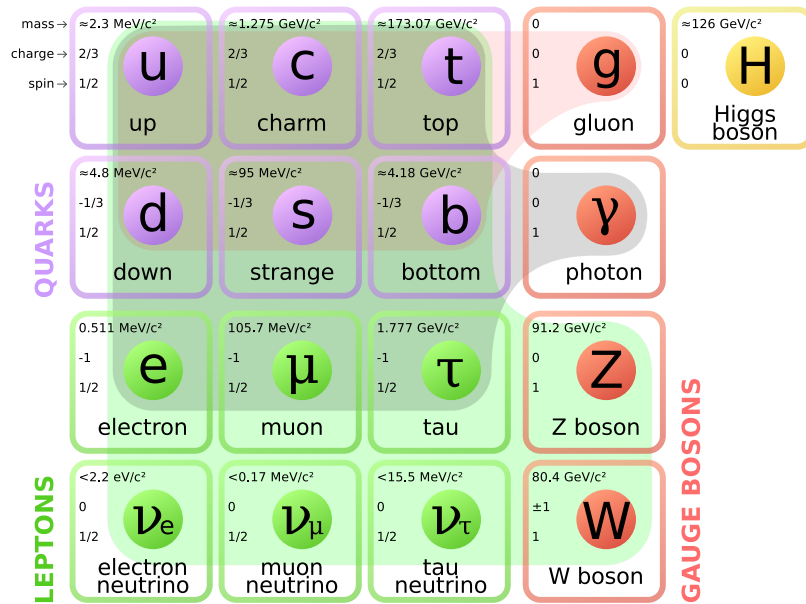


Figure 2.1.: An overview of the particles and interactions (mediated by the gauge bosons) of the Standard Model.

Source: https://commons.wikimedia.org/wiki/File:Standard_Model_of_Elementary_Particles_modified_version.svg (retrieved 2015-09-17).

their interactions and decay products. This is because, as opposed to the other fundamental interactions, the strong interaction actually increases in strength with greater distances.¹ Moreover, unlike in electromagnetism, the gauge boson mediating the strong interaction – the gluon – is itself affected by the strong interaction. If one were to attempt to separate the quarks of a hadron like the proton, the energy required would be so large that massive particle-antiparticle pairs would be created, forming new hadrons and mesons instead of providing unbound elementary quarks. In other words, the binding energy due to the strong interaction is larger than the energy required for pair-production. This phenomenon is called *confinement*. The nuclear force which binds atomic nuclei (consisting of protons and neutrons, which are hadrons) together is in fact an effective remnant of the strong force not dissimilar to the van der Waals force in molecules.

In QCD, each quark carries one of three different kinds of so-called *color charges* (hence the name), while antiquarks carry negative (or anti-)color. Gluons have both color and anti-color and can transfer color charge between particles. The coupling constant describing the strength of the interaction is denoted by α_s for the strong

¹Up to a certain point.

coupling. However, this “constant”, often called *running coupling*, actually depends on the energy scale at which a process takes place. While the coupling strength increases with larger energy scales for theories such as *quantum electrodynamics* (QED), α_s is found to diminish with higher energies. Because of this phenomenon called *asymptotic freedom*, quarks in high-energy collider experiments can be treated as asymptotically free particles, which will be exploited in chapter 3. Details on QCD can be found in many standard works, e. g. [Kan93; HM84].

Mathematically, the Standard Model is described using a gauge group for each known interaction. The full Standard Model gauge group is $SU(3)_C \times SU(2)_L \times U(1)_Y$. The different parts of that expression correspond to the strong interaction with its three color charges, treated as the gauge group $SU(3)_C$, and the electroweak interaction (which is the unification of the weak and electromagnetic interactions at the electroweak energy scale) group $SU(2)_L \times U(1)_Y$ [Mar11, ch. 1].

2.2. Supersymmetry and the Minimal Supersymmetric Standard Model

So far, no conclusive evidence of deviation from the Standard Model’s predictions has been found in particle physics experiments, even with data from the first run of the LHC at $\sqrt{s} = 8$ TeV. However, as alluded to before, questions like what dark matter consists of or the problem of gauge coupling unification at very high energy scales are reasons prompting one to consider SUSY as a step beyond the SM.

In SUSY, an additional symmetry is introduced to the Standard model relating fermions and bosons. The Lagrangian describing a supersymmetric theory is invariant (symmetric) with respect to transformations which can transform bosonic into fermionic fields and vice-versa. This means that, on a fundamental level, fermions and bosons are not treated differently by the laws and equations governing the theory. A consequence is that each Standard Model particle gains at least one superpartner whose spin differs by $1/2$. Non-Standard Model supersymmetric particles are also abbreviatedly called *sparticles*, with scalar (spin-0) sparticles being prefixed with an s- (e. g. “stop quark”) and fermionic sparticles ending in -ino (e. g. “gluino”); in formulae, they have the same symbols as SM particles but gain a tilde (e. g. a quark \tilde{q} or a gluino \tilde{g}).

A problem that arises with such an extension is that additional decay processes become available. This would include the possibility of proton decay. This, however,

has not been observed experimentally and, to the current state of knowledge, the proton is stable. To address this, the conservation of a quantity called R-parity is introduced. This multiplicative quantum number is defined as

$$P_R := (-1)^{3(B-L)+2s} \quad (2.1)$$

with the baryon number B , lepton number L and spin s .² Standard Model particles have even parity $P_R = 1$, while SUSY particles have odd parity $P_R = -1$. A consequence is that SUSY particles can only be produced or annihilated in pairs. This means that the lightest supersymmetric particle (LSP) is stable and thus a promising candidate for dark matter [Bre11, pp. 7–8].

In the most general case, this leads to an MSSM with 124 free parameters [Hab98], of which 19 correspond to the Standard Model parameters. This very large parameter space poses a significant problem for the study of SUSY, as concrete predictions can of course only be made by eventually assigning values to some parameters. Different models attempt to mitigate this issue. For example, the *constrained MSSM* (cMSSM) – or *minimal supergravity* (mSUGRA) – only has five SUSY parameters, assuming that (at the energy scale of “grand unification”, where the three interactions of the Standard Model unify through equal gauge couplings) all SUSY scalar boson masses, SUSY fermion masses and all trilinear couplings between the particles have equal values m_0 , $m_{1/2}$ and A_0 . The remaining parameters are the sign of the mass parameter $\text{sgn}(\mu)$ and $\tan(\beta)$, which pertain to the Higgs mechanism. The rest of the MSSM parameters at different energy scales are obtained using these boundary conditions in renormalization group equations [Bre11, pp. 8–9]. However, most of the cMSSM parameter space has already been exhausted experimentally.

To begin with, just like in the Standard Model,³ SUSY would imply that sparticles have equal masses to their Standard Model counterparts. However, since there has been no clear experimental evidence of SUSY yet, this cannot be the case – the sparticles, if they exist, must have larger masses than even the top quark. This means that SUSY must be a spontaneously broken symmetry. Note that for the SUSY quarks (squarks), there exist two distinct states (resulting in two “versions” of squarks with potentially different masses), just like there are two spin states for every Standard Model quark. The SUSY field squark eigenstates which take part in interactions

²(Anti-)quarks have baryon number $B = \mp \frac{1}{3}$ and (anti-)leptons have lepton number $L = \mp 1$.

³where originally, all particle flavors are mass-degenerate due to the electroweak symmetry group $SU(2)_L$

(called the “chiral eigenstates” and denoted with subscripts L and R for “left-handed” and “right-handed”)⁴ are not the same as the mass eigenstates which determine the particle masses. They are related through a phenomenon called *mixing*. This arises because the relevant SUSY Lagrangian contains bilinear combinations not only of the same states (e. g. $\tilde{q}_L \tilde{q}_L$), but also “mixed” terms like $\tilde{q}_L \tilde{q}_R$. For example, for the top squark, the situation can be written as

$$\begin{aligned} \mathcal{L}_{\text{stop masses}} &= A \tilde{t}_L \tilde{t}_L + B \tilde{t}_R \tilde{t}_R + C \tilde{t}_R \tilde{t}_L + D \tilde{t}_L \tilde{t}_R \\ &= - \begin{pmatrix} \tilde{t}_L & \tilde{t}_R \end{pmatrix} M_{\tilde{t}}^2 \begin{pmatrix} \tilde{t}_L \\ \tilde{t}_R \end{pmatrix} \end{aligned} \quad (2.2)$$

with the squared “mass matrix”

$$M_{\tilde{t}}^2 = \begin{pmatrix} A & C \\ D & B \end{pmatrix}.$$

As the mass matrix $M_{\tilde{t}}$ is not diagonal, the mass eigenstates differ from the states \tilde{t}_L and \tilde{t}_R . The off-diagonal terms are proportional to the (large) top mass m_t , which is why the mixing is significant for stops so that they have to be treated separately from the squarks of other flavors. Since the mixing effects are proportional to the mass of the corresponding Standard Model quark, they can be neglected for the lighter two quark families (u, d and c, s). Mixing between generations has also been determined to be negligible [Bre11, p. 9]. Through a change of basis in the form of a rotation matrix, the mass matrix can be diagonalized and the mass eigenstates obtained [Bre11, p. 9; Bee+10, p. 3]:

$$\begin{pmatrix} \tilde{t}_1 \\ \tilde{t}_2 \end{pmatrix} = \begin{pmatrix} \cos(\theta_{\tilde{t}}) & \sin(\theta_{\tilde{t}}) \\ -\sin(\theta_{\tilde{t}}) & \cos(\theta_{\tilde{t}}) \end{pmatrix} \begin{pmatrix} \tilde{t}_L \\ \tilde{t}_R \end{pmatrix} \quad (2.3)$$

with the mass eigenstates \tilde{t}_1, \tilde{t}_2 which are associated with the masses $m_{\tilde{t}_1}, m_{\tilde{t}_2}$. This is why the mixing angle $\theta_{\tilde{t}}$ is introduced as an important parameter in the consideration of stops. Conventionally, \tilde{t}_1 is the lower-mass state and is predicted to be the lightest of all squarks.

⁴This terminology is somewhat misleading as chirality does not apply to the scalar squarks.

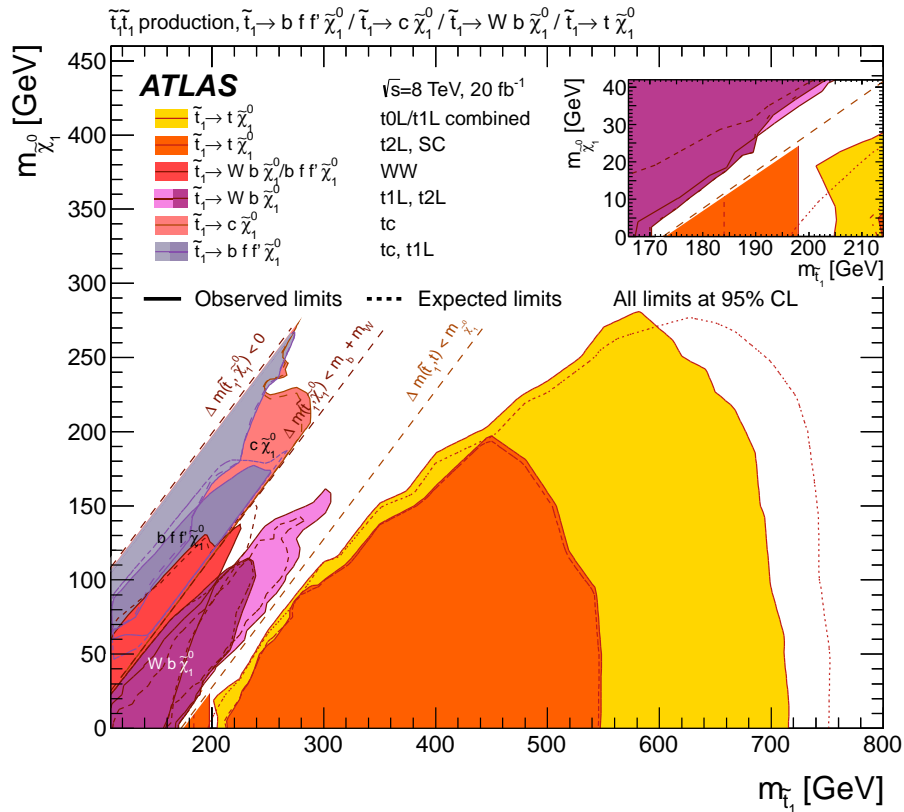


Figure 2.2.: Summary of the dedicated ATLAS searches for top squark pair-production based on 20 fb^{-1} of pp -collision data taken at $\sqrt{S} = 8 \text{ TeV}$ [ATL15].

2.3. Experimental searches and exclusion limits

As mentioned in the first chapter, many high-energy physics experiments have a goal of searching for evidence for supersymmetry. Among them are hadron collider experiments, as at the LHC. As more experimental data becomes available for rising energy scales, more and more versions of SUSY can be excluded if the observations do not agree with their predictions. At higher collider energies, production of very massive particles (including SUSY particles, if they exist) becomes increasingly likely, allowing the formulation of lower bounds on the masses of the SUSY particles if the predictions corresponding to those masses are not met in experiments.

Information and plots about the exclusion limits on SUSY parameters using current LHC data can be obtained from the ATLAS and CMS collaborations. An example is shown in fig. 2.2. Specifying a global limit on a single parameter is difficult due to the multitude of possible different decays and interactions, only some of which are

suitable to probe SUSY parameters, and the wide variation in different models used in evaluating the data (cMSSM, MSSM with different assumptions...). The exclusion limits are strongly model-dependent and a wide range of values is given for different models. A detailed discussion of the experimental approaches cannot be given here; fig. 2.2 shall only serve as motivation illustrating that the available parameter space for stop masses $m_{\tilde{t}}$ less than about 700 GeV is strongly constrained. The other mass parameters that will be studied in chapter 4 (the \tilde{t}_2 -mass, the remaining squark masses $m_{\tilde{q}}$ and the gluino mass $m_{\tilde{g}}$) are even larger than the (light) stop mass and thus have even stricter exclusion limits associated with them. A detailed summary of the consequences of the first LHC run for SUSY can be found in [Cra14]. There, generic mass limits of approximately $m_{\tilde{t}} \geq 650$ GeV, $m_{\tilde{q}} \geq 800$ GeV and $m_{\tilde{g}} \geq 1$ TeV are quoted.

2.4. Feynman diagrams and Feynman rules

In this section, the basic steps to arrive at Feynman diagrams in the quantum field theoretic formalism of canonical quantization are outlined. An alternative approach to quantum field theory is the method of path integrals (“sum over histories”). This portrayal is strongly based on [Das08], with a similar account given in [PS95, chapter 4]; this is to be understood for the entire section, such that pieces of information will not all be individually cited to [Das08; PS95]. A more intuitive approach to Feynman diagrams is presented in [Sey05].

First, a word on relativistic *quantum field theory* (QFT): The transition to a field theory and Lagrangians (instead of the Hamiltonian formalism of non-relativistic quantum mechanics) lends itself more easily to a relativistic theory. It turns out that relativistic quantum mechanics naturally lead to a many-particle theory. As such, states in QFT are states in Fock space, with a vacuum state $|0\rangle$ representing the state where no particles are present. Creation and annihilation operators a and a^\dagger (which add or remove a particle) are introduced akin to those found for the energy states of the quantum mechanic harmonic oscillator. In a process called “second quantization”, the states themselves are represented using operators which act on the vacuum state to produce a many-particle state: $|\phi\rangle = \phi|0\rangle$. Thus, after the observables were replaced by operators (“quantized”) in first quantization, now the physical states are also represented using (field) operators. Note that even relativistic QFT only incorporates special relativity, as a quantum theory of gravity is not established yet, which is a large current problem of physics.

2.4.1. Canonical quantization and the S matrix

In scattering experiments (which also comprise collider experiments), an initial set of particles with known energies and momenta is made to interact to produce a different set of particles with potentially different energies and momenta. Detailed information about the exact interaction process cannot generally be predicted and in any case is not available to the real-world observer, who can only detect the final set of particles long after the interaction has taken place. Due to this nature of scattering experiments, theoretical treatments consider *asymptotic free-particle states* long before and after the interaction processes. The central quantity to be determined is the *cross section* σ , which is a measure of the probability of a certain set of processes to occur. It is defined as the ratio of scattered particles corresponding to the given process to the flux (number of particles per unit area) of incoming particles and thus has the dimensions of $[\sigma] = \text{L}^2$ (an area), commonly given in units of $\text{b} = 10^{-28} \text{ m}^2$ (or SI-prefixed versions thereof). For comparison, if a process has a cross section of σ , its probability or rate of occurrence is the same as that of an idealized classical experiment where an incoming beam of point-like particles is directed at a target of solid disks with area σ .

In the canonical quantization formalism, the *probability amplitude* or *scattering amplitude* (which is related to the cross section) is an element of the so-called S matrix. Assuming that the incoming particles at $t \rightarrow -\infty$ as well as the outgoing particles at $t \rightarrow \infty$ can be represented using free-particle states,⁵ if the initial state is denoted

$$|i\rangle := |\psi_i(-\infty)\rangle$$

for some time-dependent state $|\psi_i(t)\rangle$, the time evolution to the point of observation of the final state at $t \rightarrow \infty$ from this state is given by the unitary time evolution operator $U(t, t_0)$ as

$$|\psi_i(\infty)\rangle = U(-\infty, \infty) |\psi_i(-\infty)\rangle = S|i\rangle$$

defining

$$S := U(-\infty, \infty). \quad (2.4)$$

In general, the time evolution operator is given (in the interaction picture) by the

⁵If necessary, this can be achieved by modifying the interaction Hamiltonian to “switch off adiabatically” such that the interaction vanishes for $t \rightarrow \pm\infty$: $H_I(t) \rightarrow \lim_{\eta \rightarrow 0} e^{-\eta|t|} H_I(t)$.

Dyson series

$$U(t, t_0) = T \exp \left(-i \int_{t_0}^t H_I(t') dt' \right) \quad (2.5)$$

with the time ordering operator T .⁶ The S matrix is thus simply the operator evolving the initial state to the final (scattered) state. Usually, the Dyson series (2.5) cannot be evaluated analytically. In this case, the S matrix can be approximated perturbatively through the expansion

$$S = \mathbb{1} + (-i) \int_{-\infty}^{\infty} H_I(t) dt + \frac{(-i)^2}{2!} \int_{-\infty}^{\infty} \int_{-\infty}^{\infty} T H_I(t) H_I(t') dt dt' + \dots \quad (2.6)$$

The probability amplitude that the scattered particle will be in the final free-particle state $|f\rangle$ is the matrix element

$$S_{fi} = \langle f | S | i \rangle .$$

This demonstrates that knowledge of the S matrix enables one to obtain information about the transition probabilities of the scattering process.

Going further in studying S matrices, *Wick's theorem* is a very important tool. It is useful to give the interaction Hamiltonian in normal-ordered form in quantum field theory. Normal ordering of an operator is defined as the order in which annihilation operators are applied before (stand to the right of) creation operators:

$$:aa^\dagger: := a^\dagger a . \quad (2.7)$$

This is relevant because the field operators can be expanded in the basis of plane wave solutions – for example, for scalar Klein-Gordon fields:

$$\phi(x) = \int \frac{1}{\sqrt{(2\pi)^3 2k^0}} \left(e^{-ik \cdot x} a(\vec{k}) + e^{ik \cdot x} a^\dagger(\vec{k}) \right) d^3k . \quad (2.8)$$

A normal-ordered operator has useful properties, among them that the *vacuum expectation value* (VEV) of a normal-ordered operator vanishes:

$$\langle 0 | :A: | 0 \rangle = 0 \quad (2.9)$$

⁶The action of the time ordering operator on a product of operators can be defined as $T \phi(x) \phi(y) := \phi(x) \phi(y) \theta(x^0 - y^0) + \phi(y) \phi(x) \theta(y^0 - x^0)$. Note that the order inside the time ordering matters for fermionic fields.

because the annihilation operators are on the very right and thus applied first, resulting in zero since they are acting on the vacuum state. This has a tangible physical interpretation, as the vacuum expectation value of any physical observable would be expected to be zero – the vacuum state contains no particles, so that there are no non-trivial properties to observe. With the Hamiltonian given in normal order, the evaluation of S matrix elements involves the time-ordered form of normal-ordered operators (recall (2.5)). Wick's theorem provides a systematic way of evaluating products of operators. One defines the contraction of two operators as

$$\overline{\phi(x)\phi(y)} := T\phi(x)\phi(y) - :\phi(x)\phi(y):; \quad (2.10)$$

since the vacuum expectation value of a normal-ordered product vanishes, the VEV of the contraction can directly be identified with that of the time-ordered product. With this, a form of Wick's theorem states that⁷

$$\begin{aligned} T \prod_{j=1}^n \phi(x_j) &= :\phi(x_1)\phi(x_2)\dots\phi(x_n): \\ &+ \overline{\phi(x_1)\phi(x_2)} :\phi(x_3)\dots\phi(x_n): + \overline{\phi(x_1)\phi(x_3)} :\phi(x_2)\dots\phi(x_n): + \dots \\ &+ \overline{\phi(x_1)\phi(x_2)} \overline{\phi(x_3)\phi(x_4)} :\phi(x_5)\dots\phi(x_n): + \dots \end{aligned} \quad (2.11)$$

or, in words, that an arbitrary time-ordered product of field operators can be written as a sum of terms with normal-ordered products on the right and all possible contractions of the field operators to the left.⁸ For the free Klein-Gordon field theory (scalar particles, i. e. spin 0), it can be shown that

$$\langle 0| T \overline{\phi(x)\phi(y)} |0\rangle = \overline{\phi(x)\phi(y)} = iG_F(x-y) \quad (2.12)$$

with the *Feynman Green's function* (or *Feynman propagator*) $G_F(x-y)$. Similar results are obtained for other theories such as Dirac fields (spin- $1/2$ particles). (2.12) hints at the relevance of both Wick's theorem, which expresses time-ordered products in terms of normal-ordered products and contractions, and the Feynman Green's function, which is related to contractions between field operators.

Green's functions (also called propagators) are solutions to linear differential equations where the inhomogeneity is a point-like source (δ -distribution). For a

⁷For bosonic field operators. Care must be taken with fermionic field operators, as each commutation introduces a factor of -1 due to the anticommutation relations.

⁸Each combination of contractions $\overline{\phi(x_i)\phi(x_j)}$ must be present exactly once in the total sum.

given linear inhomogeneous differential equation

$$L(\phi(x)) = J(x)$$

with a linear differential operator L , a solution $G(x, y)$ to the equation

$$L(G(x, y)) = -\delta^4(x - y)$$

is a Green's function for that equation. Due to the linearity of the differential operator,

$$\phi(x) = \int G(x, y)J(y)d^4y$$

is a solution to the equation. Thus, with the knowledge of the Green's function, solutions to the equation can be constructed by integrating the product of the Green's function and the inhomogeneity.⁹ With wave equations such as the Klein-Gordon equation or the Dirac equation of quantum field theory, there are generally several possible Green's functions. Two of them are the advanced and retarded Green's functions $G_A(x - y)$ and $G_R(x - y)$ which have support only in the past and future light cones, respectively.¹⁰

2.4.2. The path to Feynman diagrams

To illustrate the use of Wick's theorem, the example of a Yukawa interaction (interaction between a spin- $1/2$ Dirac field and a charge-neutral scalar field, for example protons and π^0 mesons¹¹) from [Das08, section 8.9] shall be sketched. The Lagrangian density¹² used in this theory is

$$\mathcal{L} = i\bar{\psi}\not{\partial}\psi - m\bar{\psi}\psi + \frac{1}{2}\partial_\mu\phi\partial^\mu\phi - \frac{M^2}{2}\phi^2 - g\bar{\psi}\psi\phi \quad (2.13)$$

with the four-gradient ∂^μ , $\not{\partial} = \gamma^\mu\partial_\mu$ (with the Dirac matrices γ^μ), a fermionic field ψ with mass m , a bosonic field ϕ with mass M and a coupling constant g .¹³ The

⁹If the equation has constant coefficients, G is a convolution operator $G(x, y) = G(x - y)$.

¹⁰These Green's functions are already encountered in classical wave theories such as classical electrodynamics.

¹¹The example is simplified and does not represent all properties of p - π^0 interaction.

¹²The Lagrangian density is defined by the relation $L = \int \mathcal{L}d^3x$ with the "full" Lagrangian L ; a Hamiltonian density \mathcal{H} is defined in the same manner.

¹³With the Lagrangian, the dynamical equations governing the theory can be obtained through the Euler-Lagrange equations analogously to classical mechanics.

Lagrangian is separated into free-particle and interaction terms:

$$\mathcal{L}_0 = i\bar{\psi}\not{\partial}\psi - m\bar{\psi}\psi + \frac{1}{2}\partial_\mu\phi\partial^\mu\phi - \frac{M^2}{2}\phi^2 \quad (2.14)$$

$$\mathcal{L}_1 = -g\bar{\psi}\psi\phi = -g:\bar{\psi}\psi\phi: = -\mathcal{H}_1 \quad (2.15)$$

with the interaction Hamiltonian density \mathcal{H}_1 . Now, using this concrete example, the S matrix is given by the expansion of the Dyson series (2.6):

$$\begin{aligned} S &= T \exp\left(-i \int_{-\infty}^{\infty} H_I dt\right) = T \exp\left(-i \int \mathcal{H}_1 d^4x\right) \\ &= \mathbb{1} - ig \int :\bar{\psi}(x)\psi(x)\phi(x): d^4x \\ &\quad - \frac{g^2}{2} \iint T :\bar{\psi}(x)\psi(x)\phi(x) : :\bar{\psi}(x')\psi(x')\phi(x') : d^4x d^4x' + \dots \end{aligned}$$

This can now be evaluated using Wick's theorem (2.11):

$$\begin{aligned} S &= \mathbb{1} - ig \int :\bar{\psi}(x)\psi(x)\phi(x): d^4x \\ &\quad - \frac{g^2}{2} \iint \left[:\bar{\psi}(x)\psi(x)\phi(x)\bar{\psi}(x')\psi(x')\phi(x') : \right. \\ &\quad \quad \overbrace{\phi(x)\phi(x')} : \bar{\psi}(x)\psi(x)\bar{\psi}(x')\psi(x') : \\ &\quad \quad + \overbrace{\psi_\alpha(x)\bar{\psi}_\beta(x')} : \bar{\psi}_\alpha(x)\psi_\beta(x')\phi(x)\phi(x') : \\ &\quad \quad - \overbrace{\psi_\alpha(x')\bar{\psi}_\beta(x)} : \psi_\beta(x)\bar{\psi}_\alpha(x')\phi(x)\phi(x') : \\ &\quad \quad + \overbrace{\phi(x)\phi(x')\psi_\alpha(x)\bar{\psi}_\beta(x')} : \bar{\psi}_\alpha(x)\psi_\beta(x') : \\ &\quad \quad - \overbrace{\phi(x)\phi(x')\psi_\alpha(x')\bar{\psi}_\beta(x)} : \psi_\beta(x)\bar{\psi}_\alpha(x') : \\ &\quad \quad - \overbrace{\psi_\alpha(x)\bar{\psi}_\beta(x')\psi_\beta(x')\bar{\psi}_\alpha(x)} : \phi(x)\phi(x') : \\ &\quad \quad \left. - \overbrace{\phi(x)\phi(x')\psi_\alpha(x)\bar{\psi}_\beta(x')\psi_\beta(x')\bar{\psi}_\alpha(x)} \right] d^4x d^4x' \\ &\quad + \dots \end{aligned}$$

Writing this in detail in terms of positive and negative energy operators, one obtains a sum of terms each representing a distinct physical process. Different terms of the full transition amplitude $\langle f|S|i\rangle$ can be obtained by evaluating matrix elements of the different terms in the sum. For example, for the second term at second order ($\sim g^2$)

in the expansion, a non-vanishing matrix element can be obtained if both the initial and the final state contain a proton and an anti-proton $p\bar{p} \rightarrow p\bar{p}$ (with the possibility of different momenta and spin states): $|i\rangle = |p_1, s_1; p_2, s_2\rangle$ and $|f\rangle = |q_1, s'_1; q_2, s'_2\rangle$. Denoting the aforementioned term as $S_2^{(2)}$, evaluation of this matrix element yields

$$\begin{aligned} \langle f|S_2^{(2)}|i\rangle &= \langle q_1, s'_1; q_2, s'_2|S_2^{(2)}|p_1, s_1; p_2, s_2\rangle \\ &\sim g^2 \frac{m^2}{\sqrt{p_1^0 p_2^0 q_1^0 q_2^0}} \bar{u}_\alpha(q_1, s'_1) v_\alpha(q_2, s'_2) i\tilde{G}_F(p_1 + p_2) \bar{v}_\beta(p_2, s_2) u_\beta(p_1, s_1). \end{aligned} \quad (2.16)$$

This process can be physically interpreted to correspond to a $p\bar{p}$ pair annihilating to produce a π^0 meson, which in turn pair-produces another $p\bar{p}$ pair. $\tilde{G}_F(k)$ is the Fourier transform of the (scalar)¹⁴ Feynman propagator G_F which, in this example theory, has the form

$$\tilde{G}_F(k) = \lim_{\varepsilon \rightarrow 0} \frac{i}{k^2 - M^2 + i\varepsilon}. \quad (2.17)$$

The transition amplitude (2.16) depends on the coupling constant g to the order of the perturbative expansion, the masses M^2 (through the propagator) and m^2 and the observable momenta and spin states before and after the process through the spinors of the incoming and outgoing particles.

Now, although Wick's theorem is very helpful in evaluating the perturbative expansion of S matrix elements, it is somewhat cumbersome to work with directly. Finally, this is where Feynman diagrams come in: They provide a graphical notation for the different terms in the Wick expansion. Incoming and outgoing particles corresponding to the initial and final states are represented as external lines (one for each particle) entering a graph. The propagators are represented as internal particle lines, as they are completely independent of the initial and final states. Lastly, the third element of Feynman diagrams are vertices. These represent the interaction itself and stem from the interaction Lagrangian \mathcal{L}_I . Given these three categories of elements, the transition amplitudes can be found by drawing all possible Feynman diagrams corresponding to terms of a desired order in the perturbative expansion. The calculation of each diagram is then done by simply including different factors in the term which directly correspond to the different elements (external lines, propagators and vertices) in the diagram. The prescriptions describing which element

¹⁴The fermions have a different Feynman propagator associated with them which appears in terms where intermediate (virtual) fermions are generated (those which contain the contraction of fermionic field operators).

corresponds to which mathematical expression are known as the Feynman rules of the theory (see also section 2.5).

To summarize, Feynman diagrams are a systematic way to perturbatively evaluate scattering matrix elements and thus transition probabilities for scattering experiments. Different terms that come about in the perturbative expansion of the S matrix correspond to the vertices and propagators that are compiled in the Feynman rules of a theory, with higher orders in perturbation corresponding to more complex diagrams (with higher numbers of vertices).

2.5. SUSY-QCD Feynman rules

The Feynman rules for ordinary Standard Model QCD are given in [AH13, appendix Q; PS95, appendix A.1; DGR04, pp. 88–89]; the additional rules for SUSY-QCD can be found in [DGR04; Bee+97, p. 50].¹⁵ They are usually given in momentum space, simplifying calculations. For external (incoming or outgoing) lines, the following rules apply:

- For each fermion or anti-fermion entering the graph with four-momentum p and spin state s , the spinor

$$u(p, s) \quad \text{or} \quad \bar{v}(p, s), \quad (2.18)$$

respectively, is to be included as a factor to the scattering amplitude.

- For each fermion or anti-fermion leaving the graph with four-momentum p' and spin state s' , the spinor

$$\bar{u}(p', s') \quad \text{or} \quad v(p', s'), \quad (2.19)$$

respectively, is to be included as a factor to the scattering amplitude.

- For each gluon entering or leaving the graph with momentum k , the polarization vector

$$\varepsilon(k, \lambda) \quad \text{or} \quad \varepsilon^*(k, \lambda), \quad (2.20)$$

respectively, is to be included as a factor to the scattering amplitude.

¹⁵The notation in different sources is not always consistent, which has been accounted for.

In Standard Model QCD, two types of propagators exist: A quark and a gluon propagator. For these, the following factors are to be included:

$$\text{---}\blacktriangleright\text{---} = \frac{i}{\not{p} - m} = i \frac{\not{p} + m}{p^2 - m^2} \quad (2.21)$$

$$\text{-----} = \frac{i}{k^2} \left(-g^{\mu\nu} + (1 - \xi) \frac{k^\mu k^\nu}{k^2} \right) \delta^{ab} \quad (2.22)$$

with the quark mass and momentum p and m , the gluon momentum k , a gauge ξ (which can be chosen to be 1 – this will be done in calculations), $\not{p} = \gamma^\mu p_\mu$ and the Dirac matrices γ^μ . Finally, three kinds of vertices are possible:

$$\begin{array}{c} \bar{q} \\ \nearrow \\ \bullet \\ \nwarrow \\ q \end{array} \begin{array}{c} g \\ \text{-----} \\ \mu, a \end{array} = -ig_s T^a \gamma^\mu \quad (2.23)$$

$$\begin{array}{c} k_2, b \\ \nearrow \\ \bullet \\ \nwarrow \\ k_1, a \end{array} \begin{array}{c} g \\ \text{-----} \\ \mu \\ \text{-----} \\ g \\ \text{-----} \\ \nu \end{array} \begin{array}{c} g \\ \text{-----} \\ k_3, c \\ \leftarrow \end{array} = -g_s^2 f^{abc} \left[g_{\mu\nu} (k_1 - k_2)_\lambda + g_{\nu\lambda} (k_2 - k_3)_\mu + g_{\lambda\mu} (k_3 - k_1)_\nu \right] \quad (2.24)$$

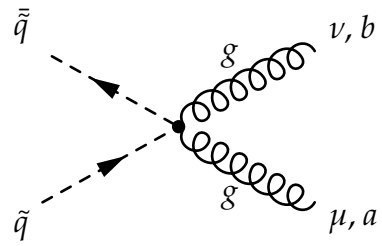
$(k_1 + k_2 + k_3 = 0)$

and a four-gluon vertex $\sim g_s^2$, where $T^a = \frac{1}{2}\lambda^a$ with the Gell-Mann matrices λ^a and $(T^a)^{bc} = -if^{abc}$ with the SU(3) structure constants f^{abc} .

For SUSY-QCD, propagators for squarks and gluinos as well as a number of vertices are added to the existing ones. The squark propagator is simply that for a free scalar particle, cf. (2.17). The following of these will be relevant for leading-order calculations of $\tilde{t}\tilde{t}^*$ -production:

$$\text{-----}\blacktriangleright\text{-----} = \frac{i}{p^2 - m^2} \quad (2.25)$$

$$\begin{array}{c} \bar{q} \\ \nearrow \\ p_2 \\ \nwarrow \\ p_1 \\ \nearrow \\ \tilde{q} \end{array} \begin{array}{c} g \\ \text{-----} \\ \mu, a \end{array} = -ig_s T^a (p_1 - p_2)^\mu \quad (2.26)$$



$$= ig_s^2 \{T^a, T^b\} g^{\mu\nu} \quad (2.27)$$

with squark momenta p, p_1 and p_2 and the squark mass m .

3. Stop quark pair-production

As the name suggests, hadron colliders like the LHC operate by accelerating hadrons up to great energies (TeV-scale) and directing these beams of accelerated hadrons into each other. These collisions are analyzed by large detectors at specific points around the accelerator. Due to the high-energy collisions of many particles, a multitude of physical interaction processes occurs, potentially producing unstable, high-mass intermediate particles which decay through different channels into more stable products. It is these final products which are analyzed using different types of detectors designed for different collision products (charged, uncharged, low-mass, high-mass...). Together with very sophisticated data processing, the types, amounts, energies and trajectories of the resultant particles are used to reason about the interactions that take place during the collisions.

Since free quarks cannot be experimented on or directly observed due to confinement, proton-proton (pp)¹ collisions are studied instead. The LHC operates as such a pp -collider. As protons are not elementary particles, it is not sufficient to merely determine the cross section of a direct interaction between quarks or gluons (*partons*) to produce SUSY particles – one has to consider the elementary particle content of the protons to proceed from the cross sections for “direct” QCD interactions (partonic cross sections) to the full hadronic cross sections. These can then be compared with experimental results.

Here, only (SUSY-)QCD contributions are considered for the calculations. While QED processes will of course be present as well, their contributions are negligible for these purposes in the context of a hadron collider such as the LHC. At the TeV energy scale, the electromagnetic coupling constant α is much smaller than the QCD coupling $\alpha_s \gg \alpha$. Moreover, top quarks are excluded from the initial state throughout the analysis. Due to its large mass ($m_t = (173.34 \pm 0.76)$ GeV [ATL14]), the top quark is extremely unlikely to be present in the initial state at all so that its contribution to the colliding protons (the parton distribution function) is practically zero [MSTW08]. On the other hand, the lighter quark masses (all masses other than m_t) will be taken

¹or proton-antiproton ($p\bar{p}$)

to be $m_q \approx 0$. This can be justified because the masses of the light quarks (on the order of a few MeV to GeV) are dwarfed by the masses of the SUSY particles, which must be at least in the TeV range due to experimental exclusion limits (see section 2.3).

3.1. Stop quark production at leading order

In this section, two-to-two particle interactions will be studied. In general, the momenta of the incoming (initial-state) particles will be labeled p_1 and p_2 , while those of the outgoing (final-state) particles will be labeled q_1 and q_2 . When evaluating Feynman diagrams, the so-called *Mandelstam variables*

$$\begin{aligned} s &:= (p_1 + p_2)^2 = (q_1 + q_2)^2 \\ t &:= (p_1 - q_1)^2 = (p_2 - q_2)^2 \\ u &:= (p_1 - q_2)^2 = (p_2 - q_1)^2 \end{aligned} \quad (3.1)$$

are usually introduced. \sqrt{s} is the center-of-mass energy of the incoming particles, while t and u are related to the momentum transfer in scattering processes where the interaction is mediated by particle exchange.² Additionally, the shorthands

$$\begin{aligned} t_1 &:= t - m_{\tilde{q}}^2 \\ u_1 &:= u - m_{\tilde{q}}^2 \end{aligned} \quad (3.2)$$

with the squark mass $m_{\tilde{q}}$ will be useful. The Mandelstam variables are related through

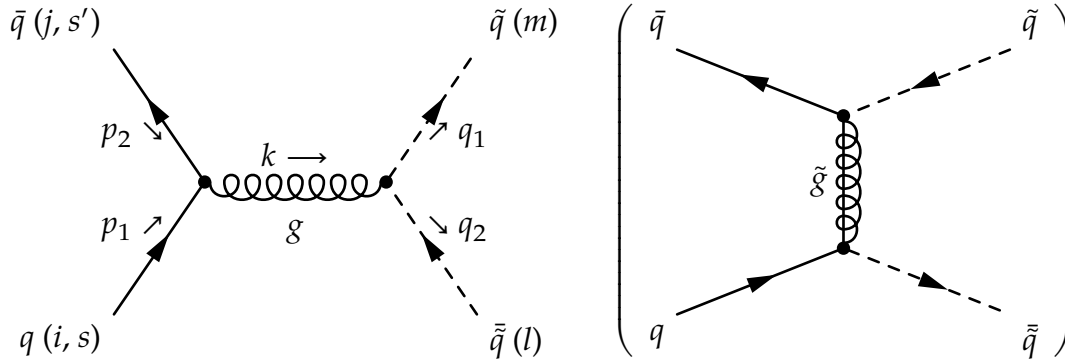
$$s + t + u = p_1^2 + p_2^2 + q_1^2 + q_2^2 = 2m_{\tilde{q}}^2, \quad (3.3)$$

due to four-momentum conservation.³

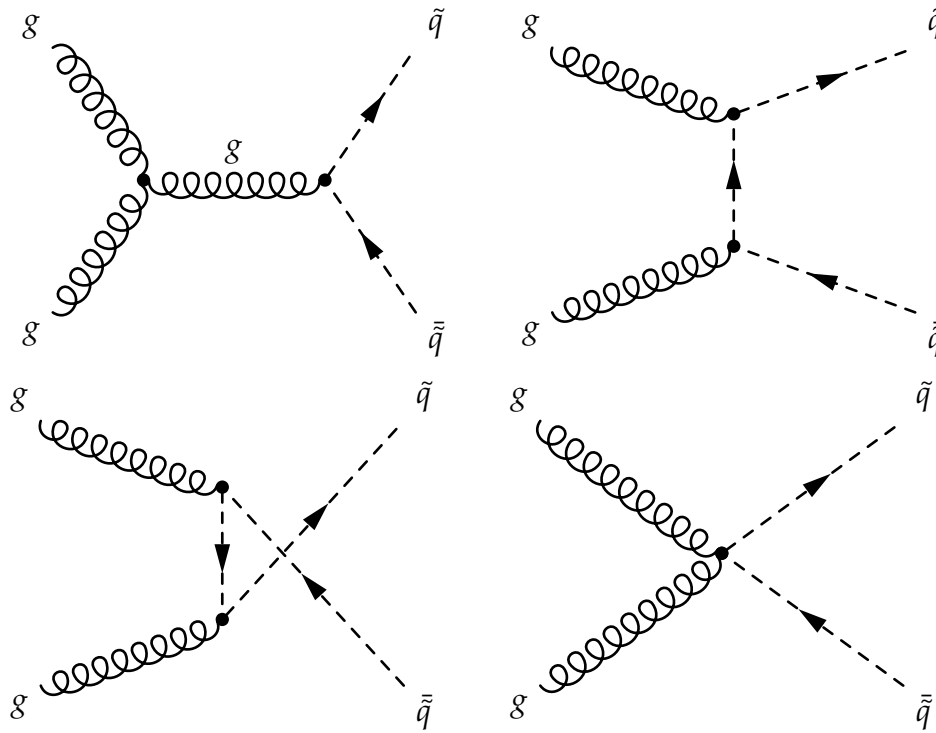
For squark pair-production in general, one has to consider all Feynman diagrams which are proportional to the coupling strength $\alpha_s = \frac{g_s^2}{4\pi}$ (i. e. in first order), consistent with the Feynman rules of (SUSY-)QCD and which result in a squark and a corresponding antiparticle as output products. The two processes exhibiting squark pair-production at leading order are $q\bar{q}$ -annihilation and gg -fusion.

²Cf. the second and third diagram in fig. 3.1b.

³The second equality follows because all possible initial-state particles (light quarks and gluons) are taken to have vanishing mass ($p_1^2 = p_2^2 = 0$) and $q_1^2 = q_2^2 = m_{\tilde{q}}^2$ because only final-state $\tilde{q}\bar{\tilde{q}}$ -pairs are considered here.



(a) Diagrams for $q\bar{q}$ -annihilation. In the first diagram, color (i, j, l, m) and spinor (s, s') indices as well as four-momenta are explicitly labeled. Note that the diagram in parentheses does not contribute to stop-production.



(b) Diagrams for gg -fusion.

Figure 3.1.: Feynman diagrams for supersymmetric quark pair-production at leading order. Cf. also [Bee+97, p. 6].

3.1.1. Production processes and matrix elements

The Feynman diagrams contributing to $\tilde{q}\tilde{q}^*$ -production at leading order are shown in fig. 3.1. As mentioned before, initial-state top quarks are excluded. Due to this, the second Feynman diagram (parenthesized) in fig. 3.1a does not contribute to the calculations. This is because the strong interaction conserves flavor and thus, if top squarks are to be produced at the vertices in the diagram, the incoming particles must be a top-antitop pair as well. The second and third diagram in fig. 3.1b are identical except for the exchange of the outgoing (or, equivalently, incoming) particles. The reason that this is a separate Feynman diagram is that the two gluons in the initial state are indistinguishable particles. The squark propagator introduces a factor $\sim k^{-2}$, with the momentum k depending on the external momenta due to conservation. Depending on which of the two diagrams is viewed, k is composed differently from the momenta of the (distinguishable) final-state squarks so that the propagator introduces a factor proportional to either $1/t$ (“ t -channel”) or $1/u$ (“ u -channel”), necessitating the treatment of both diagrams.

As an example for the evaluation of such a Feynman diagram and the calculation of a transition amplitude, a more detailed account of the first diagram in fig. 3.1a shall be given here. In the diagram, the color and spinor indices to be used for the calculation as well as the four-momenta (defined to be $p_1 + p_2 = k = q_1 + q_2$) are labeled. Using the Feynman rules from section 2.5, one obtains

$$\begin{aligned} iM &= \bar{v}(p_2, s')(-ig_s T^a \gamma^\mu)u(p_1, s) \left(-\frac{i}{k^2} g_{\mu\nu} \delta_{ab} \right) (-ig_s T^b (q_1 - q_2)^\nu) \\ &= i \frac{g_s^2}{s} T_{ji}^a T_{ml}^a \gamma_{\beta\alpha}^\mu (q_1 - q_2)_\mu \bar{v}_\beta(p_2, s') u_\alpha(p_1, s). \end{aligned}$$

Employing the identity [DGR04, p. 89; PS95, appendix A.3]

$$T_{ij}^a T_{kl}^a = \frac{1}{2} \delta_{il} \delta_{kj} - \frac{1}{2N} \delta_{ij} \delta_{kl}, \quad (3.4)$$

with $N = 3$ for the three color charges of $SU(N) = SU(3)$, this yields

$$iM = i \frac{g_s^2}{s} \left(\frac{1}{2} \delta_{jl} \delta_{im} - \frac{1}{2N} \delta_{ij} \delta_{lm} \right) \gamma_{\beta\alpha}^\mu (q_1 - q_2)_\mu \bar{v}_\beta(p_2, s') u_\alpha(p_1, s).$$

It can be observed that the scattering amplitude M depends on the color and spinor indices i, j, l, m, s, s' : $M = M_{ijlm,ss'}$. Since the initial color and spin states can differ

for every individual interaction in hadron collisions, the desired quantity is the cross section where an averaging over all such possible initial states has been performed.

Here, the sum of all transition probabilities $\sum |M|^2 = \sum_{i,j,l,m,s,s'} M_{ijlm,ss'}$ shall be determined, with the averaging (division by the number of possible initial states) to be performed in the transition from matrix elements to cross sections in section 3.1.2. In this case, the sum of the transition probabilities gives

$$\begin{aligned} \sum |M|^2 &= \frac{g_s^4}{s^2} \left(-\frac{1}{2N} \delta_{ij} \delta_{lm} + \frac{1}{2} \delta_{im} \delta_{jl} \right)^2 \gamma_{\beta\alpha}^\mu \gamma_{\delta\epsilon}^\sigma (q_1 - q_2)_\mu (q_1 - q_2)_\sigma \\ &\quad \times \bar{v}_\beta(p_2, s') u_\alpha(p_1, s) \bar{u}_\delta(p_1, s) v_\epsilon(p_2, s'). \end{aligned}$$

It can easily be shown that

$$\left(-\frac{1}{2N} \delta_{ij} \delta_{lm} + \frac{1}{2} \delta_{im} \delta_{jl} \right)^2 = \frac{NC_F}{2}$$

with $C_F = \frac{N^2-1}{2N} = \frac{4}{3}$. Using this and the identities [PS95, appendices A.2, A.3]

$$\sum_s u_\alpha(p, s) \bar{u}_\beta(p, s) = \not{p}_{\alpha\beta} + m_q \delta_{\alpha\beta} \quad (3.5)$$

$$\sum_s v_\alpha(p, s) \bar{v}_\beta(p, s) = \not{p}_{\alpha\beta} - m_q \delta_{\alpha\beta} \quad (3.6)$$

$$\gamma_{\beta\alpha}^\mu \gamma_{\alpha\delta}^\nu \gamma_{\delta\epsilon}^\rho \gamma_{\epsilon\beta}^\sigma = \text{Tr}(\gamma^\mu \gamma^\nu \gamma^\rho \gamma^\sigma) = 4(g^{\mu\nu} g^{\rho\sigma} - g^{\mu\rho} g^{\nu\sigma} + g^{\mu\sigma} g^{\nu\rho}) \quad (3.7)$$

it follows that⁴

$$\sum |M|^2 = 2 \frac{g_s^4}{s^2} NC_F (2p_1 \cdot (q_1 - q_2) p_2 \cdot (q_1 - q_2) - (q_1 - q_2)^2 p_1 \cdot p_2)$$

with the four-vector inner product $x \cdot y = x^\mu y_\mu$. Rewriting the scalar products in terms of the Mandelstam variables, one obtains the form given in (3.8).

The final results for the summed square matrix elements for all relevant processes at leading order are

$$\sum |M_{\text{LO}}|^2 [q\bar{q} \rightarrow \tilde{q}\tilde{q}] = 4g_s^4 NC_F \frac{t_1 u_1 - m_{\tilde{q}}^2 s}{s^2} \quad (3.8)$$

$$\sum |M_{\text{LO}}|^2 [gg \rightarrow \tilde{q}\tilde{q}] = 2g_s^4 \left[C_O \left(1 - 2 \frac{t_1 u_1}{s^2} \right) - C_K \right] \left[1 - 2 \frac{sm_{\tilde{q}}^2}{t_1 u_1} \left(1 - \frac{sm_{\tilde{q}}^2}{t_1 u_1} \right) \right] \quad (3.9)$$

with $C_O = N(N^2 - 1) = 24$ and $C_K = \frac{N^2-1}{N} = 2C_F = \frac{8}{3}$. As explained above, these

⁴recall $m_q \approx 0$

sums have lost any dependence on color or spinor indices. They only depend on the parameters ($m_{\tilde{q}}$ in this case) and the Mandelstam variables s, t_1, u_1 . For reference, equivalent results can be found in [Bee+97, p. 7].⁵

3.1.2. Partonic cross sections

Having obtained the squared matrix elements, it is possible to proceed to cross sections. The former still depend on the momenta of incoming and outgoing particles via the Mandelstam variables s, t and u . However, since the goal is to calculate the total cross sections, the details of neither the individual scattering angles nor the distribution of momentum and energy between the final-state particles is of any concern – only the energy of the colliding protons is well-defined in a hadron collider so that all possible final states shall be considered. The task is to continue from the transition probabilities (3.8) to the differential cross section (depending on e. g. the scattering angle) and the total cross section.

These cross sections can be obtained by performing the Lorentz-invariant phase-space integration as outlined in [Ros09, section 9]. If one considers two-to-two particle scattering, as is done here, the whole interaction takes place in a plane and can thus be described using only one scattering angle ϑ , being independent of the second angle φ . To obtain the differential cross section, it is useful in this case to perform calculations in the center-of-mass reference frame using the scattering angle. As the (total) cross sections are the same in all reference frames (Lorentz scalars), it is permissible to use an arbitrary frame. Having found a result, however, the transformation back to the Mandelstam variables is advisable – contrary to the scattering angles, which are frame-dependent, they are Lorentz-invariant. For two final-state particles at leading order, the differential partonic cross section in a form depending on t can then be found to be⁶ [Bee+97, p. 8]

$$\frac{d\sigma^{(p)}}{dt} = \frac{1}{16\pi s^2} K_{ij} \theta(s - 4m_{\tilde{q}}^2) \theta((t - q_2^2)(u - q_2^2) - q_2^2 s) \sum |M(s, t)|^2. \quad (3.10)$$

Here, the first step function ensures that particles cannot be produced without the necessary collision energy \sqrt{s} (energy conservation). The factor K_{ij} finally performs

⁵The results presented in [Bee+97] must be divided by 2 (because only the production of $\tilde{t}_1 \bar{\tilde{t}}_1$ and not $\tilde{t}_2 \bar{\tilde{t}}_2$ is to be evaluated) and n_f must be set to 1 (since only one flavor is considered here) to reproduce (3.8) and (3.9).

⁶The dependence on u can be eliminated, see below.

the remaining work for the averaging of the possible initial color and spin states (previously, the transition probabilities were simply summed up). It is given by

$$K_{ij} = \begin{cases} \frac{1}{4N^2} & \text{for } q\bar{q} \text{ initial state} \\ \frac{1}{4(N^2-1)^2} & \text{for } gg \text{ initial state} \end{cases}. \quad (3.11)$$

Now, one arrives at the total cross section from (3.10) by integrating over the remaining invariant t .

Using the relation for the Mandelstam variables in (3.3), u can be expressed in terms of the other two variables as $u = 2m_{\tilde{q}}^2 - s - t$ to yield

$$\sigma^{(p)}(s) = \frac{1}{16\pi s^2} K_{ij} \theta(s - 4m_{\tilde{q}}^2) \int_{t_-}^{t_+} \sum |M(s, t)|^2 dt. \quad (3.12)$$

where the limits t_{\pm} for the integration are derived from the second step function in (3.10). In general, denoting the masses of the incoming particles as m_1, m_2 and those of the outgoing particles as m_3, m_4 , they are [Ros09, p. 38]

$$t_{\pm} = m_1^2 + m_2^2 - 2p_1^0 q_1^0 \pm |\vec{p}_1| |\vec{q}_1|; \quad (3.13)$$

in this case (cf. [Max14, p. 17]):

$$t_{\pm} = m_{\tilde{q}}^2 - \frac{s}{2} \pm \frac{1}{2} \sqrt{(s - 2m_{\tilde{q}}^2)^2 - 4m_{\tilde{q}}^4}. \quad (3.14)$$

The partonic cross sections for squark pair-production at leading order can thus be determined to be

$$\sigma_{\text{LO}}^{(p)}[q\bar{q} \rightarrow \tilde{q}\tilde{q}^*] = \frac{\alpha_s^2 \pi}{s} \frac{2}{27} \beta^3 \quad (3.15)$$

$$\sigma_{\text{LO}}^{(p)}[gg \rightarrow \tilde{q}\tilde{q}^*] = \frac{\alpha_s^2 \pi}{s} \left[\beta \left(\frac{5}{48} + \frac{31m_{\tilde{q}}^2}{24s} \right) + \left(\frac{2m_{\tilde{q}}^2}{3s} + \frac{m_{\tilde{q}}^4}{6s^2} \right) \ln \left(\frac{1-\beta}{1+\beta} \right) \right] \quad (3.16)$$

with $\beta = \sqrt{1 - \frac{4m_{\tilde{q}}^2}{s}}$. These results are identical to those given in [Bee+98, p. 3; Bee+10, p. 4]. Since the second Feynman diagram in fig. 3.1a has been excluded, they are valid only either for stop pair-production (since the massive top quarks have been excluded as initial-state particles), or in the limit of large gluino masses [Bee+98, p. 3].

As can be seen in (3.15) and (3.16), the leading-order cross section for stop quark pair-production depends solely on one parameter: the (lighter) stop mass $m_{\tilde{t}_1}$. As such, analyzing the parameter space at leading order is simple (even after proceeding to hadronic cross sections, see section 3.1.3): The cross section need only be calculated as a function of the single unknown parameter $m_{\tilde{t}_1}$.

3.1.3. Hadronic cross sections

The cross section (3.12) only describes processes where two “free” quarks or gluons interact. However, as explained before, in hadron colliders like the LHC, protons are made to collide. Protons are not elementary particles and contain not only three “valence quarks” uud , but also “sea quarks” (quark-antiquark pairs) and gluons due to the strong interaction taking place within them. Since only the momentum P and energy $\frac{\sqrt{s}}{2}$ (half the collider center-of-mass energy each) of the protons is known, it is not clear how the momentum is split up among their parton constituents, so the remaining variable s in the cross section (3.12) is not fixed. To address this, the parton momenta are expressed as $p_i = x_i P$ with the fraction of the total momentum x_i , $0 \leq x_i \leq 1$. This leads to $s = x_1 x_2 S$ ($s \sim p_1 \cdot p_2$) [Max14].

The distribution of partons within the proton is described by *parton distribution functions* (PDFs) $f_i(x_i)$, giving the probability or density of a parton i with a momentum fraction of x_i . These can be inferred from scattering experiments (deep-inelastic scattering) and have been determined at different orders of α_s in [MSTW08].⁷

The hadronic cross sections are then obtained by integrating the partonic cross sections over the possible momentum fractions x_1 and x_2 , including the PDFs for the respective incoming partons and the partonic cross sections. Thus, all possible combinations of input momenta are considered and the cross sections of each scenario summed up. The result is a convolution of the PDFs with the partonic cross sections [Bee+97, p. 36; MSTW08, p. 9]:

$$\sigma(S) = \sum_{i,j} \int_0^1 \int_0^1 f_i(x_1) f_j(x_2) \sigma_{ij}^{(p)}(s = x_1 x_2 S) dx_1 dx_2, \quad i, j \in \{u, d, c, s, b, g\}, \quad (3.17)$$

where $\sigma_{ij}^{(p)}$ is the partonic cross section with incoming partons i and j (quarks or gluons, excluding top quarks).

⁷An updated set of PDFs has since been released [MMHT14], but these new results have only been incorporated for leading-order calculations in this work. The impact from the difference between these PDF sets is not expected to be very significant here.

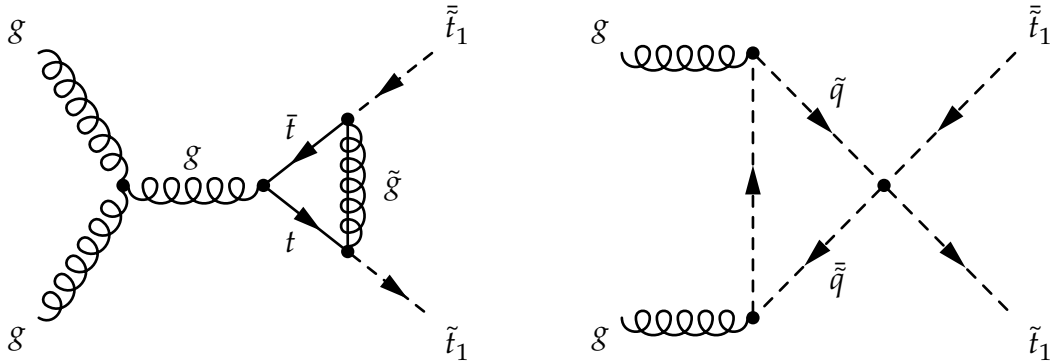


Figure 3.2.: Exemplary Feynman diagrams for processes at next-to-leading order demonstrating the involvement of additional parameters. Mixed pairs (e. g. $\tilde{t}_1\tilde{t}_2$) can also be produced in these processes.

3.2. Next-to-leading order

An analytical derivation of the (partonic) cross sections for stop pair-production in next-to-leading order is beyond the scope of this work; for an analytical discussion of these cross sections see [Bee+98]. The NLO cross sections were obtained numerically using the program Prospino [BHS96] and are presented in section 4.2. Still, a small overview of the NLO corrections shall be given here, revealing why these cross sections involve four additional SUSY parameters.⁸

Figure 3.2 shows two examples of Feynman diagrams for processes at next-to-leading order. It is immediately obvious that the gluino mass $m_{\tilde{g}}$ becomes a relevant parameter in such processes since the gluino propagator appears in the first diagram. Additionally, the mixing angle $\theta_{\tilde{t}}$ becomes relevant due to the quark-squark-gluino vertex. In the second diagram, arbitrary intermediate squark-antisquark pairs can be produced to the left of the four-squark vertex. Because of this, all possible squark masses enter into the cross section as parameters. Since the masses of squark flavors other than stop are taken to be degenerate here, this results in two parameters: The heavier stop mass $m_{\tilde{t}_2}$ and the remaining squark masses $m_{\tilde{q}}$.

⁸Assuming degenerate squark masses $m_{\tilde{q}}, \tilde{q} \neq \tilde{t}, \tilde{t}$. Without this assumption, the number of parameters would of course increase strongly – two parameters for the two mass eigenstates of each squark flavor in the general case, plus potential mixing parameters. For a discussion of non-degenerate squark masses, see [Max14].

4. Numerical analysis and results

The computation of the cross sections was carried out using the results developed in chapter 3. For leading order, C++ code was written using the [MSTW08] PDFs and the VEGAS Monte Carlo algorithm [Lep78] to perform the numerical integration to obtain the hadronic cross sections (3.17). These results were compared to the output from the Prospino [BHS96] code. At next-to-leading order, Prospino was employed exclusively to calculate the cross sections for different points in the parameter space. Prospino works in a similar manner to the C++ code as it was modified to use the [MSTW08] PDFs as well and also made use of the VEGAS algorithm. All calculations were done for a proton-proton collider with energy $\sqrt{S} = 13 \text{ TeV}$, reflecting the current operation of the LHC.

Both the C++ code and Prospino used the value of the light stop mass parameter $m_{\tilde{t}_1}$ for the energy scale, i. e. $Q = m_{\tilde{t}_1}$ – which is used both for the renormalization scale in the coupling α_s as well as the factorization scale that has to be specified for the PDFs. Code and data to compute the value of the running coupling $\alpha_s(Q)$ at different energy scales are part of the [MSTW08] and [MMHT14] code. An exemplary plot of the values obtained using this method is shown in fig. 4.1. An illustration of the PDFs themselves is given in fig. 4.2. The PDFs are provided for $10^{-6} \leq x \leq 1$ and an energy scale $1 \text{ GeV}^2 \leq Q^2 \leq 10^9 \text{ GeV}^2$.

4.1. Leading order

As detailed above, LO results were obtained using C++ code created for this work and Prospino. The number of VEGAS calls was chosen to be 200 000, resulting in relative numerical errors $\Delta\sigma/\sigma < 6 \times 10^{-5}$ for almost all data points. Prospino was set to use 10 000 VEGAS calls for all LO calculations, which gave errors $< 2.5 \times 10^{-4}$. The results are shown in fig. 4.3. Since the leading-order calculations are comparatively not very computationally demanding and only depend on one free parameter, the entire extent of the LO space can be easily sampled with fine granularity. From

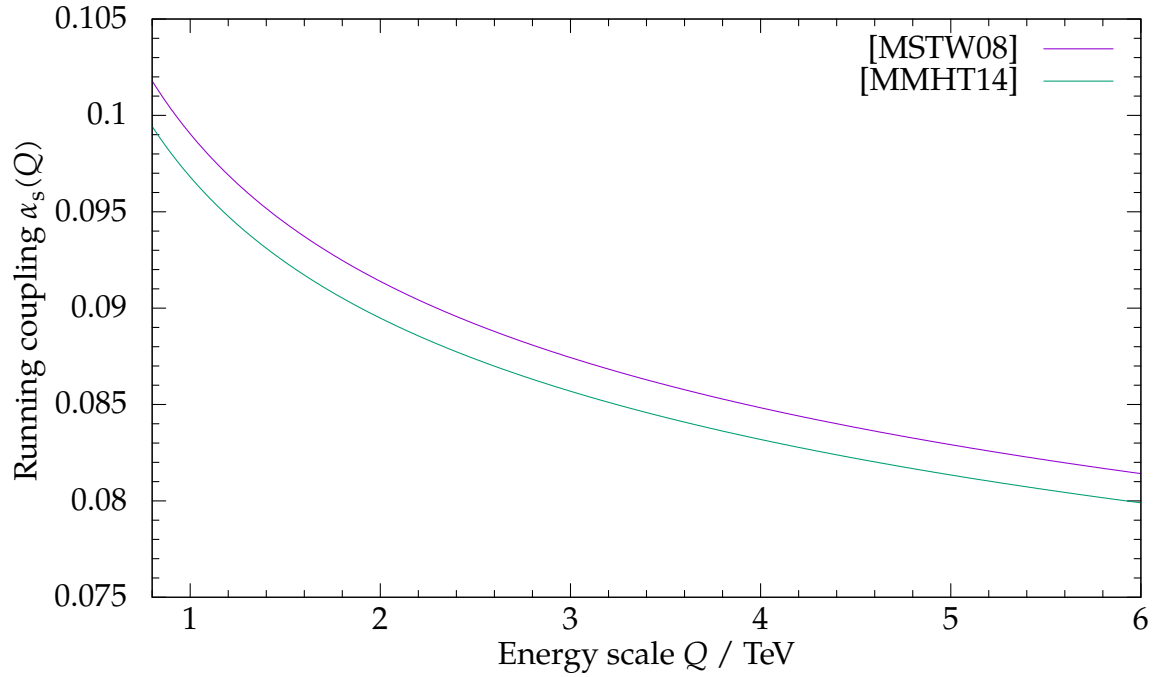


Figure 4.1.: Values of the running coupling α_s (leading order) generated using code and data from [MSTW08] and [MMHT14].

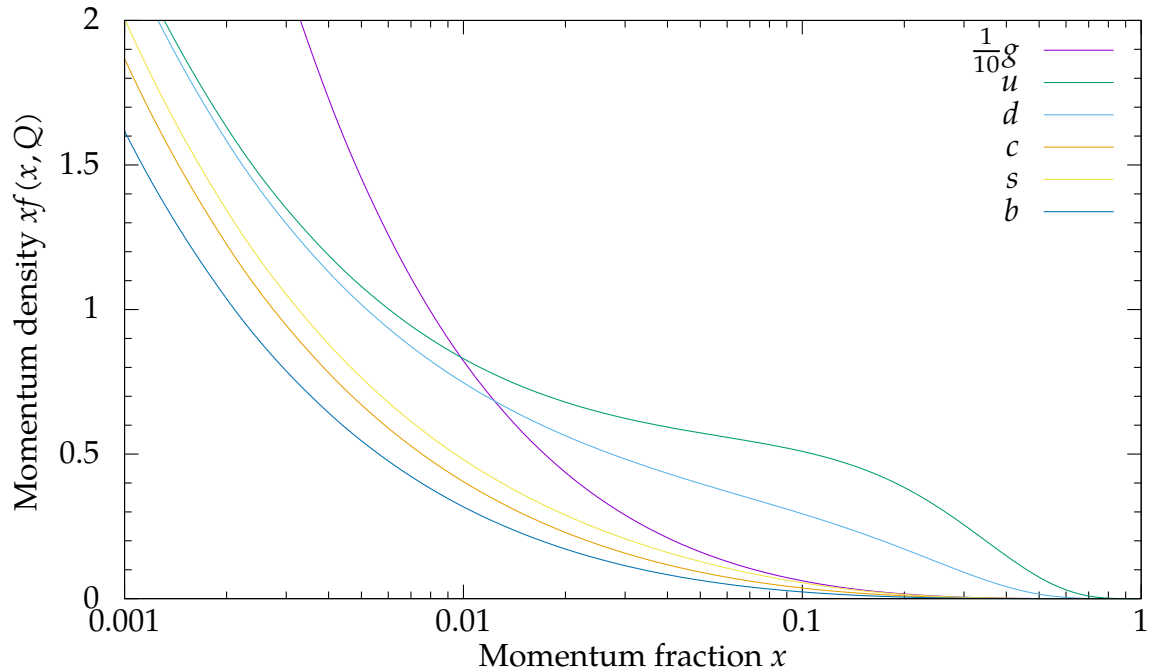


Figure 4.2.: Illustration of the parton distribution functions (PDFs) $f_i(x, Q)$ from [MSTW08] at leading order. The energy scale Q was chosen to be 1.5 TeV. The gluon distribution has been scaled for illustration purposes. Antiquarks are not shown (other than \bar{u} and \bar{d} , they are identical to the quark PDFs).

energy conservation, stops with masses up to $\frac{\sqrt{s}}{2} = 6.5$ TeV could be produced at the LHC, although it is expected that the LHC can effectively probe SUSY up to a scale of about 3 TeV. As expected and as visible in fig. 4.3, the cross section drops sharply with increasing values of $m_{\tilde{t}_1}$, ranging from 2.05×10^{-2} pb at 800 GeV to less than 10^{-18} pb at masses > 5.5 TeV, at some point becoming experimentally infeasible. In the middle of the figure (between 2 TeV to 4 TeV), the dependence of σ on the mass might roughly be exponential. For very large masses > 5 TeV, the (relative) rate of decrease even seems to grow.

For comparison, the same calculations have been carried out using both the [MSTW08] and the [MMHT14] PDFs using the C++ code. Up to masses of about 3 TeV, the difference is barely noticeable. However, the (relative) deviation grows with larger masses, with the [MMHT14] set resulting in lower total cross sections. The difference seems largely due to the difference in values of α_s used (see fig. 4.1). The exact details behind this discrepancy were not pursued further, as the main focus lay not on the comparison of the different PDF sets, but on the behavior of $\tilde{t}\bar{\tilde{t}}$ -production with the SUSY parameters. For the masses realistically available for probing by the LHC, the difference is not taken to be significant. For further details on the background and data behind different PDF sets, the reader is referred to the referenced reports.

4.2. Scan of the parameter space at next-to-leading order

4.2.1. Approach

Since the light stop mass $m_{\tilde{t}_1}$ is the only parameter relevant at leading order, it is expected that it will affect the cross section much more strongly than those parameters that enter only the next-to-leading order corrections. This is confirmed in the following results. Due to this, it is not very useful to treat $m_{\tilde{t}_1}$ equally to the remaining parameters. As the cross section depends much more strongly on $m_{\tilde{t}_1}$, any contribution from the variation of the other parameters is quickly dwarfed by even small changes in $m_{\tilde{t}_1}$.

Different techniques to intelligently sample the parameter space have been considered. In the end, a “manual” approach of generating data points mainly along the parameter axes, with broad sampling of the remaining orthogonal space was

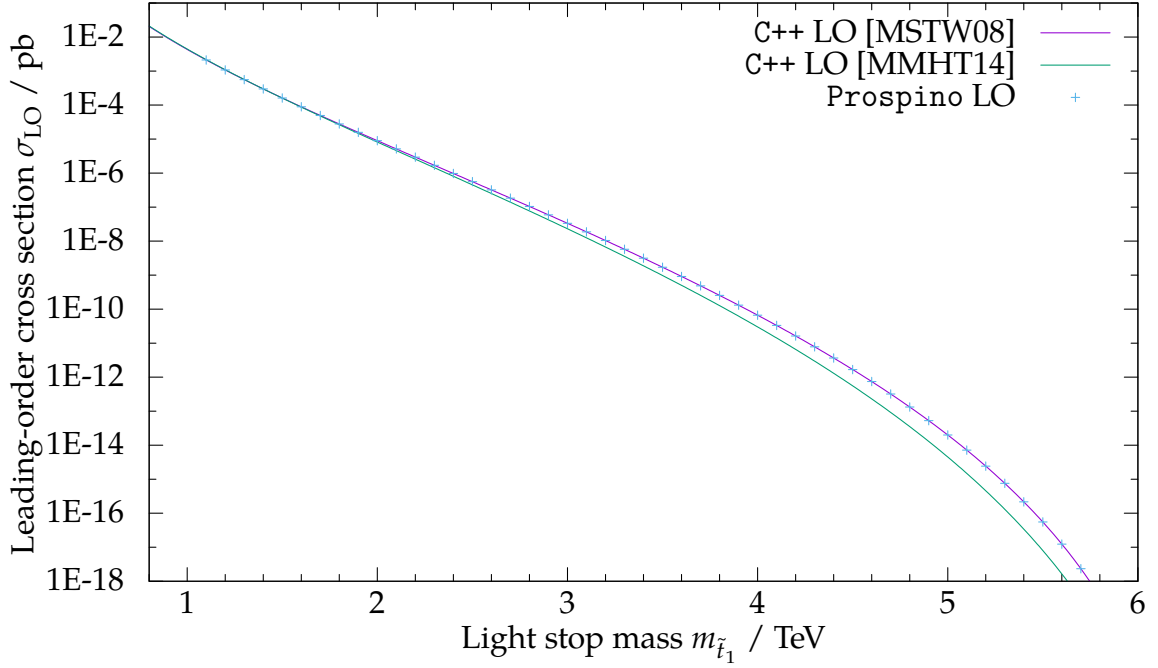


Figure 4.3.: Numerically calculated cross sections for $\tilde{t}_1\bar{\tilde{t}}_1$ -pair-production at leading order using code written for this work and using Prospino for comparison.

employed. General or sophisticated approaches to handling a large parameters space such as Markov Chain Monte Carlo (MCMC) methods exist; another possibility would be heuristics such as randomly sampling and observing the gradient (rate of change) of the cross section to choose potentially interesting trajectories. However, the space under study here was deemed of appropriate size and predictable enough that the following method was found to be suitable: For each of the parameters, the cross section's dependence is analyzed by varying this parameter in rather fine steps. For each data point, however, the other parameters are sampled in a broad interval as well. In order to constrain the computational complexity, the step sizes along these free parameters was coarser – with N parameters, the effort of generating all data points where each parameter can independently assume M values scales as M^N . As no specialized hardware was used for computations, this was necessary to ward off the “curse of dimensionality” of computational complexity.

Having generated this data, the minimum, maximum and average values at each value of the parameter under study are determined, giving a “sleeve” enveloping the average cross section. This sleeve is an estimation and also a lower bound of how much the cross section can vary when varying a certain parameter with the other

parameters being free and assuming arbitrary values. As explained above, the light stop mass was excluded since it dominates the contribution from other parameters. Instead of including it in the “variation interval”, it was set to a number of fixed values and the rest of the parameters were studied individually at these fixed points.

The number of VEGAS calls was chosen to be 10 000 for LO and 20 000 for NLO calculations, resulting in relative numerical errors $< 3 \times 10^{-4}$ for the total cross sections. The number of calls to the integration routine directly influences the numerical error on the results, but also the amount of time it takes to generate each data point. One difficulty in the computations was that the NLO cross sections seem to contain a pole or other anomaly at $m_{\tilde{q}} = m_{\tilde{g}}$ that Prospino is unable to handle. Due to this, the parameters were always chosen such that $m_{\tilde{q}} \neq m_{\tilde{g}}$, with a 5 GeV difference in cases where they would otherwise have been set to equal values.

4.2.2. Results

The average evolution of the respective parameter under study will be shown using a single line, while the range of variation in the cross section due to the free variation of the other parameters will be shown as a filled curve. The results focusing on $m_{\tilde{t}_1}$ are given in fig. 4.4. The expectation that this parameter affects the cross section much more than the others is confirmed. The variation due to the other parameters is barely visible as the cross section quickly drops over several orders of magnitude. The variation due to the rough sampling of the other parameters while varying $m_{\tilde{t}_1}$ is much smaller than the overall correction from calculating the NLO terms. The behavior of the LO and NLO cross sections appears to be very similar over a large range of values, with the difference between the two decreasing at larger stop masses. This is to be expected as α_s decreases with higher energy scales, causing higher-order corrections to shrink. Due to the similar behavior, the range of values is similar to the LO case (2.8×10^{-2} pb at 800 GeV to less than $< 10^{-18}$ pb). However, the NLO corrections are quite significant in size, e. g. a 36.6 % increase over the LO cross section at 800 GeV. The NLO corrections are always positive in this case, indicating larger cross sections. The parameter variation affected the cross section ranging from values 1.4 % lower to 2.2 % higher than the average at the low-mass end and 3.8 % lower to 3.2 % higher at the high-mass end. Because the difference between LO and NLO diminished at higher stop masses, the variation due to the parameters became more significant at those scales.

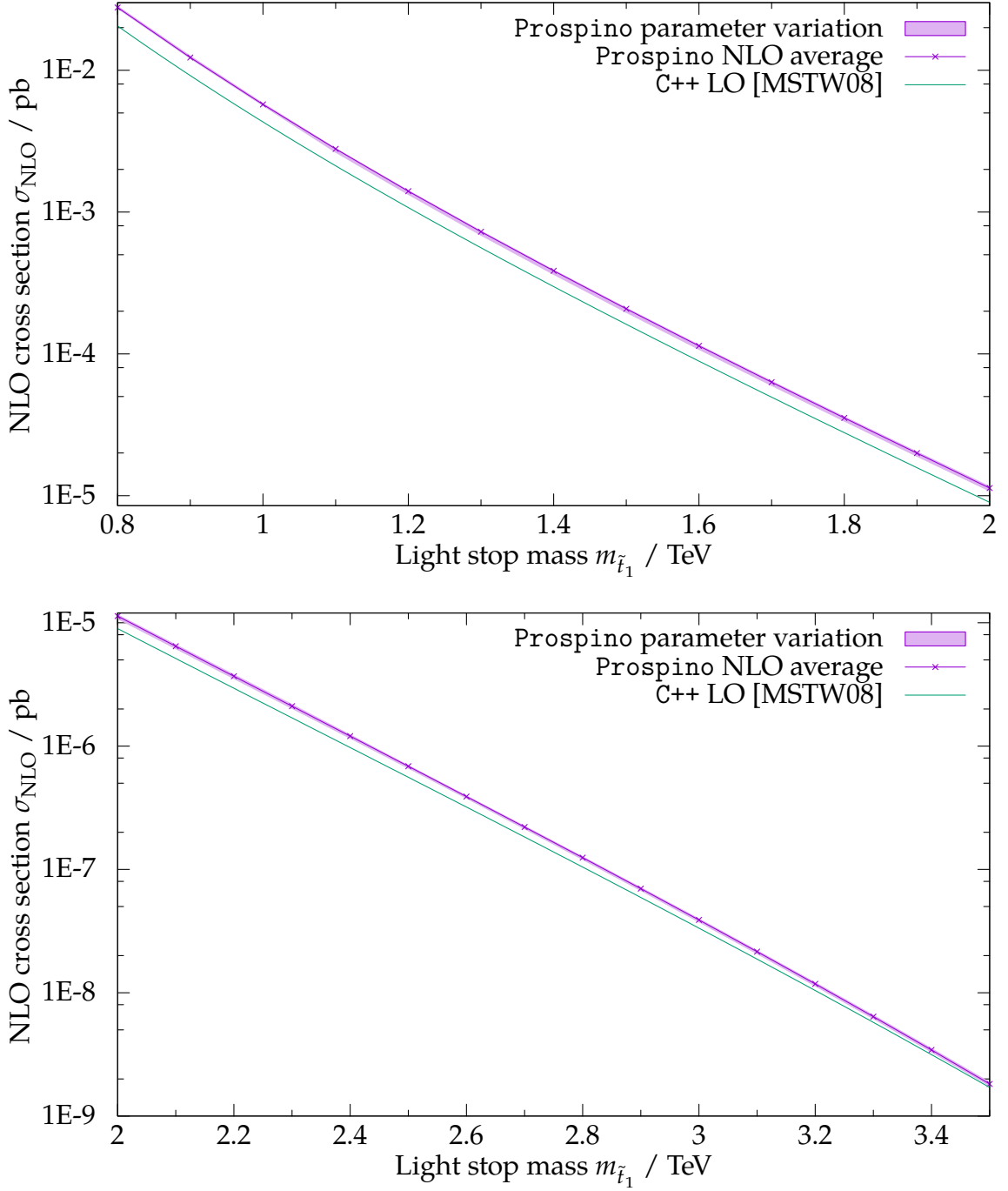


Figure 4.4.: NLO cross sections using Prospino, focusing on the parameter $m_{\tilde{t}_1}$. The filled curve gives the variation of the cross section when independently varying $m_{\tilde{t}_2}$, $m_{\tilde{q}}$, $m_{\tilde{g}}$ from 1 TeV to 10 TeV (step size 1.5 TeV) and $\sin(2\theta_{\tilde{t}})$ from -1 to 1 (step size 0.25), while the solid line represents the average over all data points. Note that the data points < 1 TeV show a slightly smaller envelope as those data points have been sampled with coarser step sizes than given above.

On the next few pages, the results for the NLO cross sections computed using Prospino [BHS96] when varying the other four parameters ($m_{\tilde{t}_2}$, $m_{\tilde{q}}$, $m_{\tilde{g}}$, $\sin(2\theta_{\tilde{t}})$) are displayed (figs. 4.5 to 4.8). Note that all figures using the same value of $m_{\tilde{t}_1}$ are to the same scale to allow for comparison. Since these parameters enter the cross section only at next-to-leading order, it is expected to depend on them much less than on the light stop mass $m_{\tilde{t}_1}$, which is already relevant at leading order. As $m_{\tilde{t}_1}$ affects the cross sections much more strongly, it would not be useful to show the variation of the cross section with this parameter varying freely – its contribution would completely dominate any effects caused by the other parameters. As such, the cross sections were calculated at three fixed values of $m_{\tilde{t}_1} = 1 \text{ TeV}, 2 \text{ TeV}$ and 3 TeV . The dependence on each parameter was plotted individually, with the remaining three parameters varying freely and being probed at a broad range of values. At $m_{\tilde{t}_1} = 1 \text{ TeV}$, the cross section was found to vary between $5.65 \times 10^{-3} \text{ pb}$ and $5.9 \times 10^{-3} \text{ pb}$; at 2 TeV and 3 TeV , the ranges were $1.06 \times 10^{-5} \text{ pb}$ to $1.17 \times 10^{-5} \text{ pb}$ and $3.74 \times 10^{-8} \text{ pb}$ to $4.05 \times 10^{-8} \text{ pb}$.

Observing the results in detail, the cross section was found to hardly depend on $m_{\tilde{t}_2}$ at all (fig. 4.5), remaining practically constant regardless of its specific value at all three scales. Subsequently, the envelope around the practically flat average was rather large compared to the curves for the other parameters in all cases, indicating that the bulk of change in the cross section is determined by those parameters and not $m_{\tilde{t}_2}$. The fact that the edges of the envelope are also practically flat (horizontal) shows that $m_{\tilde{t}_2}$ does not seem to interact with the other parameters very strongly, either, showing no indication of poles, resonances or other effects brought about by specific configurations of several parameters.

Results for $m_{\tilde{q}}$ are displayed in fig. 4.6. The variation of $m_{\tilde{q}}$ affects the cross section only for smaller values. The cross section reaches a minimum along the $m_{\tilde{q}}$ axis which is shifted to larger values with larger $m_{\tilde{t}_1}$; it is partially cut off at $m_{\tilde{t}_1} = 1 \text{ TeV}$ (i. e. located at $m_{\tilde{q}} \leq 1 \text{ TeV}$), lies at 1.8 TeV for $m_{\tilde{t}_1} = 2 \text{ TeV}$ (affecting the average cross section by about 0.7% compared to the flat curve at high $m_{\tilde{q}}$) and at 2.6 TeV for $m_{\tilde{t}_1} = 3 \text{ TeV}$ (affecting the average cross section by about 0.8%). For values of $m_{\tilde{q}}$ larger than 3 TeV to 4 TeV , the parameter's contribution increasingly becomes negligible as the average curve flattens out. This is to be expected, as producing particles with masses of 10 TeV at the LHC is very unlikely. The squarks become “decoupled” from the interactions at such masses, meaning that processes involving them can mostly be ignored.

The cross section seems to depend most strongly on $m_{\tilde{g}}$ (disregarding $m_{\tilde{t}_1}$). The

relevant results are shown in fig. 4.7. Especially for $m_{\tilde{t}_1} \geq 2$ TeV, it exhibits strong variation for $m_{\tilde{g}} \leq 3$ TeV to 4 TeV, reaching first a minimum, quickly rising to a maximum and then stabilizing somewhat below the maximum. This quick variation (along with some seemingly erratic behavior which is hinted at in the transition from minimum to maximum) is in fact due to a singularity in the NLO cross section at the stop-decay threshold

$$m_{\tilde{t}_1} = m_{\tilde{g}} + m_t \quad (m_t = 173.34 \text{ GeV}), [\text{Bee+10, p. 11}].$$

At higher values, the contribution again becomes weak, similar to the other mass parameters. As in the squark mass case, the gluinos are decoupled at masses > 10 TeV, causing the dependence of the cross section on their mass to level out. Due to the large variation of the cross section with $m_{\tilde{g}}$, it appears that the variation envelopes around the curves for the other parameters are completely dominated by the $m_{\tilde{g}}$ contribution. This is also demonstrated by the fact that the envelopes around the curves for $m_{\tilde{g}}$ are much smaller than those for the other parameters, showing that the $m_{\tilde{g}}$ variation is indeed what caused larger envelopes for other parameters (and is of course absent in the $m_{\tilde{g}}$ plots).

The dependence on $\sin(2\theta_{\tilde{t}})$ rather weak (fig. 4.8), especially at larger values for $m_{\tilde{t}_1}$, where its effects appear similarly negligible as those of $m_{\tilde{t}_2}$. For $m_{\tilde{t}_1} = 1$ TeV, however, a larger contribution was seen from this parameter, perhaps indicating a stronger influence for lower stop masses. For that choice of $m_{\tilde{t}_1}$, the envelope showed a qualitatively very different progression than at the higher values, deviating quite a bit from the behavior of the average line. While for large absolute values of $\sin(2\theta_{\tilde{t}})$ the variation due to the other parameters became quite large, indicating a stronger effect from them, a value around zero (for the positive deviation) or around 0.3 (for the negative deviation) minimized the envelope. The cross section ranged from $5.77 \times 10^{-3}{}^{+1.5\%}_{-1.2\%}$ pb at the left edge ($\sin(2\theta_{\tilde{t}}) = -1$) to $5.74 \times 10^{-3}{}^{+0.3\%}_{-0.7\%}$ pb ($\sin(2\theta_{\tilde{t}}) = 0$) and $5.736 \times 10^{-3}{}^{+0.4\%}_{-0.6\%}$ pb ($\sin(2\theta_{\tilde{t}}) = 0.3$). The general behavior was also somewhat different for the higher values of $m_{\tilde{t}_1}$: While the cross section generally decreased with rising $\sin(2\theta_{\tilde{t}})$ at 1 TeV, it increased slightly for 2 TeV and 3 TeV instead. The curve always seemed to have a small ‘‘bulge’’ around 0, indicating a change in curvature.

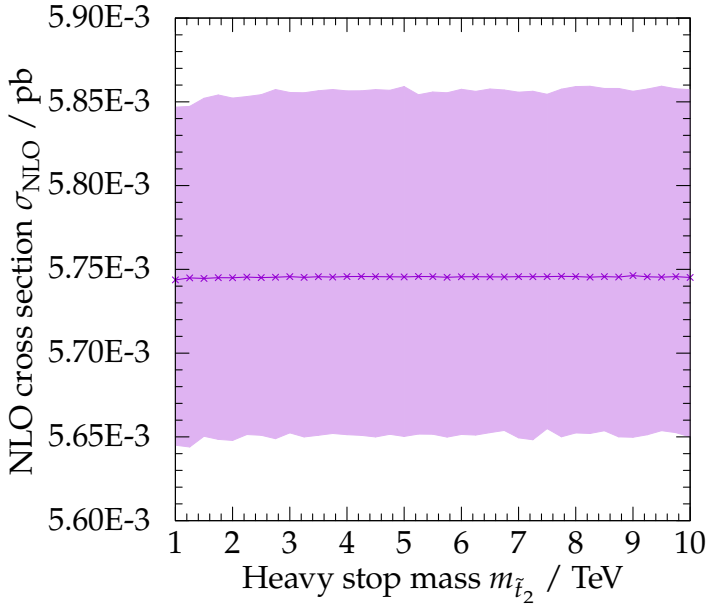
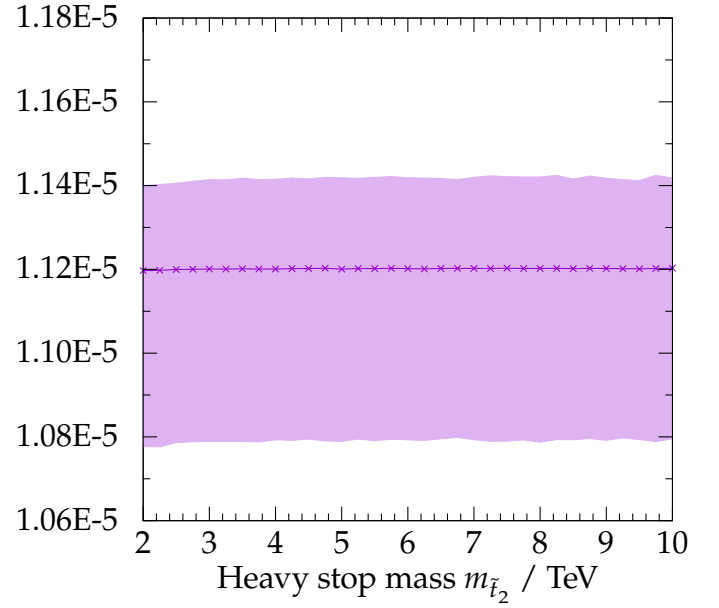
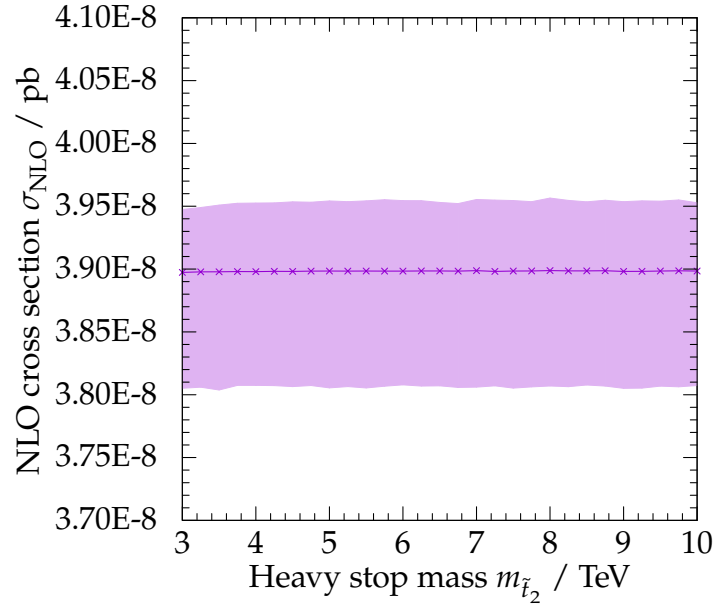
(a) Cross sections for $m_{\tilde{t}_1} = 1$ TeV.(b) Cross sections for $m_{\tilde{t}_1} = 2$ TeV.(c) Cross sections for $m_{\tilde{t}_1} = 3$ TeV.

Figure 4.5.: NLO cross sections using Prospino, focusing on the parameter $m_{\tilde{t}_2}$. The filled curve gives the variation of the cross section when independently varying $m_{\tilde{q}}$, $m_{\tilde{\chi}}$ from 1 TeV to 9 TeV (step size 4 TeV) and $\sin(2\theta_{\tilde{t}})$ from -1 to 1 (step size 0.5), while the solid line represents the average over all data points.

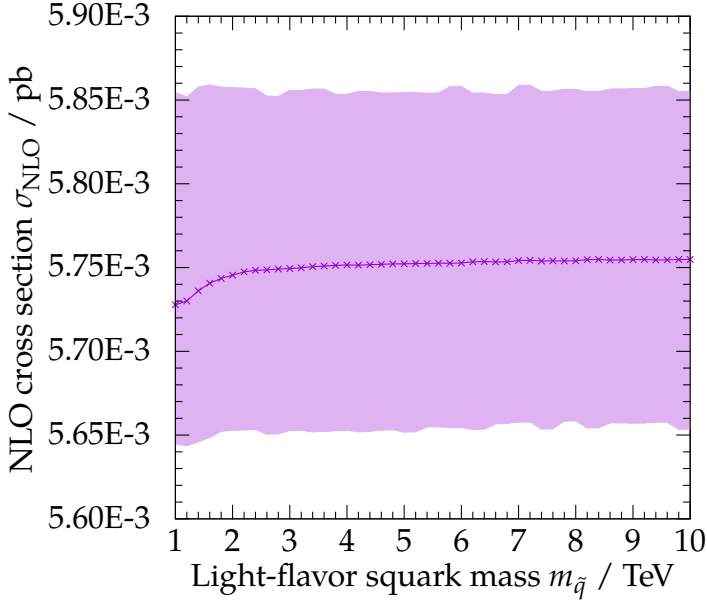
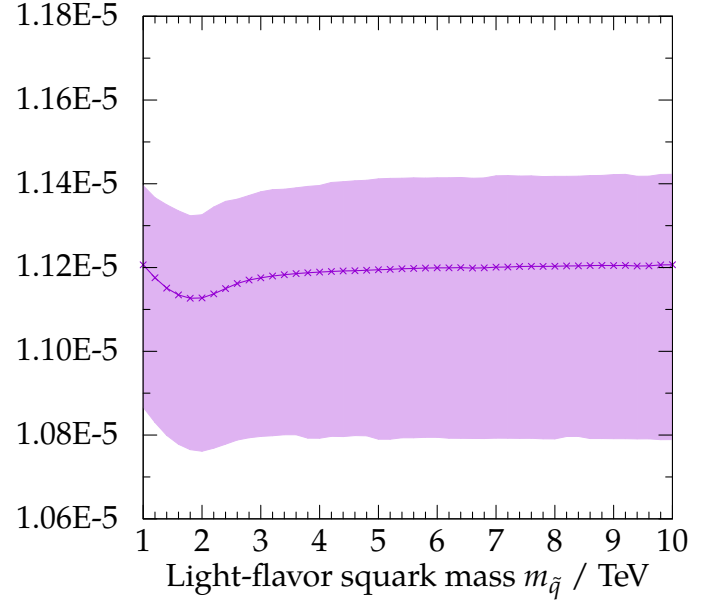
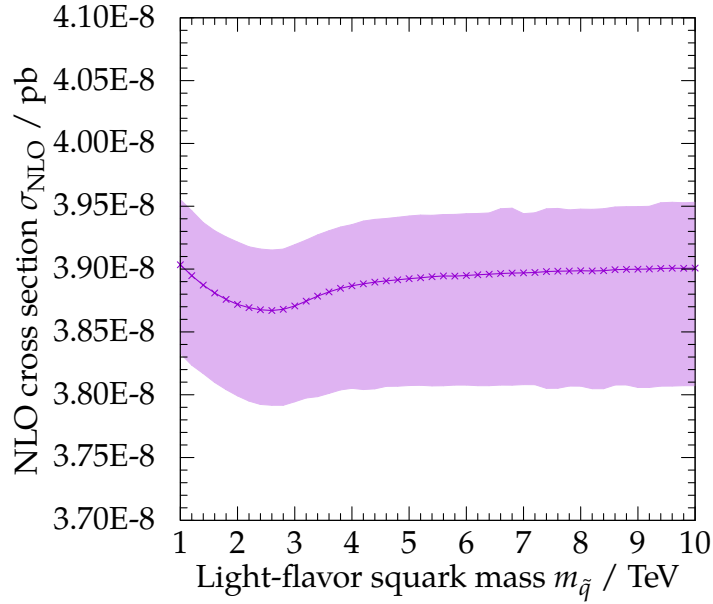
(a) Cross sections for $m_{\tilde{t}_1} = 1$ TeV.(b) Cross sections for $m_{\tilde{t}_1} = 2$ TeV.(c) Cross sections for $m_{\tilde{t}_1} = 3$ TeV.

Figure 4.6.: NLO cross sections using Prospino, focusing on the parameter $m_{\tilde{q}}$. The filled curve gives the variation of the cross section when independently varying $m_{\tilde{t}_2}$, $m_{\tilde{g}}$ from 1 TeV to 9 TeV (step size 4 TeV) and $\sin(2\theta_{\tilde{t}})$ from -1 to 1 (step size 0.5), while the solid line represents the average over all data points.

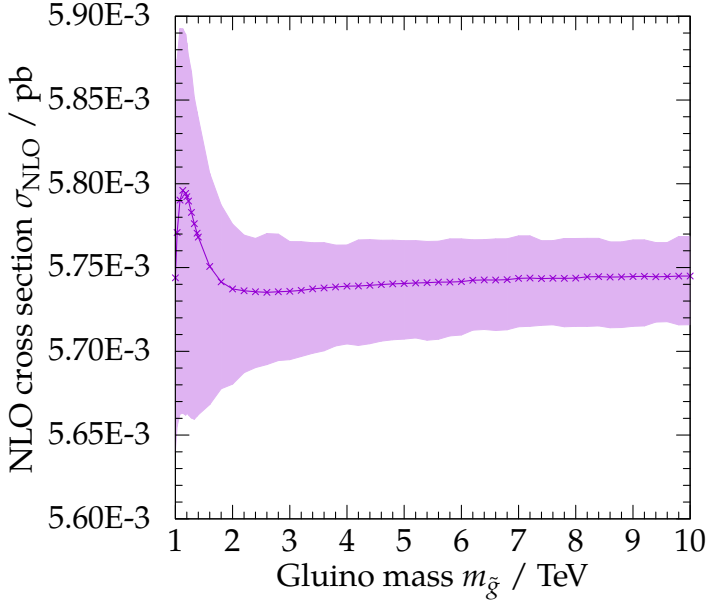
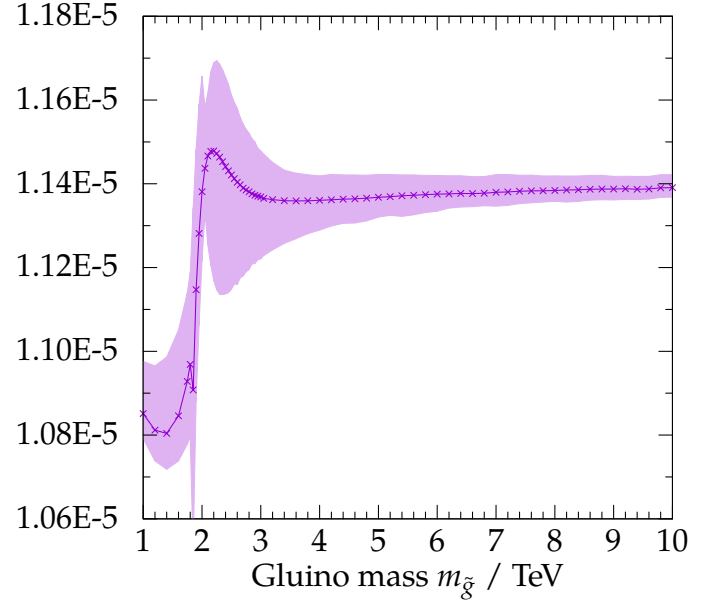
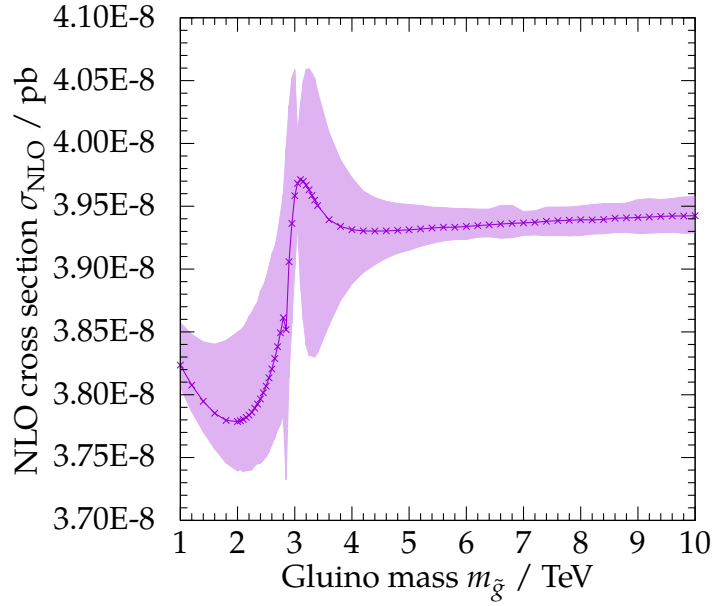
(a) Cross sections for $m_{\tilde{t}_1} = 1$ TeV.(b) Cross sections for $m_{\tilde{t}_1} = 2$ TeV.(c) Cross sections for $m_{\tilde{t}_1} = 3$ TeV.

Figure 4.7.: NLO cross sections using Prospino, focusing on the parameter $m_{\tilde{g}}$. The filled curve gives the variation of the cross section when independently varying $m_{\tilde{t}_2}$, $m_{\tilde{q}}$ from 1 TeV to 9 TeV (step size 4 TeV) and $\sin(2\theta_{\tilde{t}})$ from -1 to 1 (step size 0.5), while the solid line represents the average over all data points.

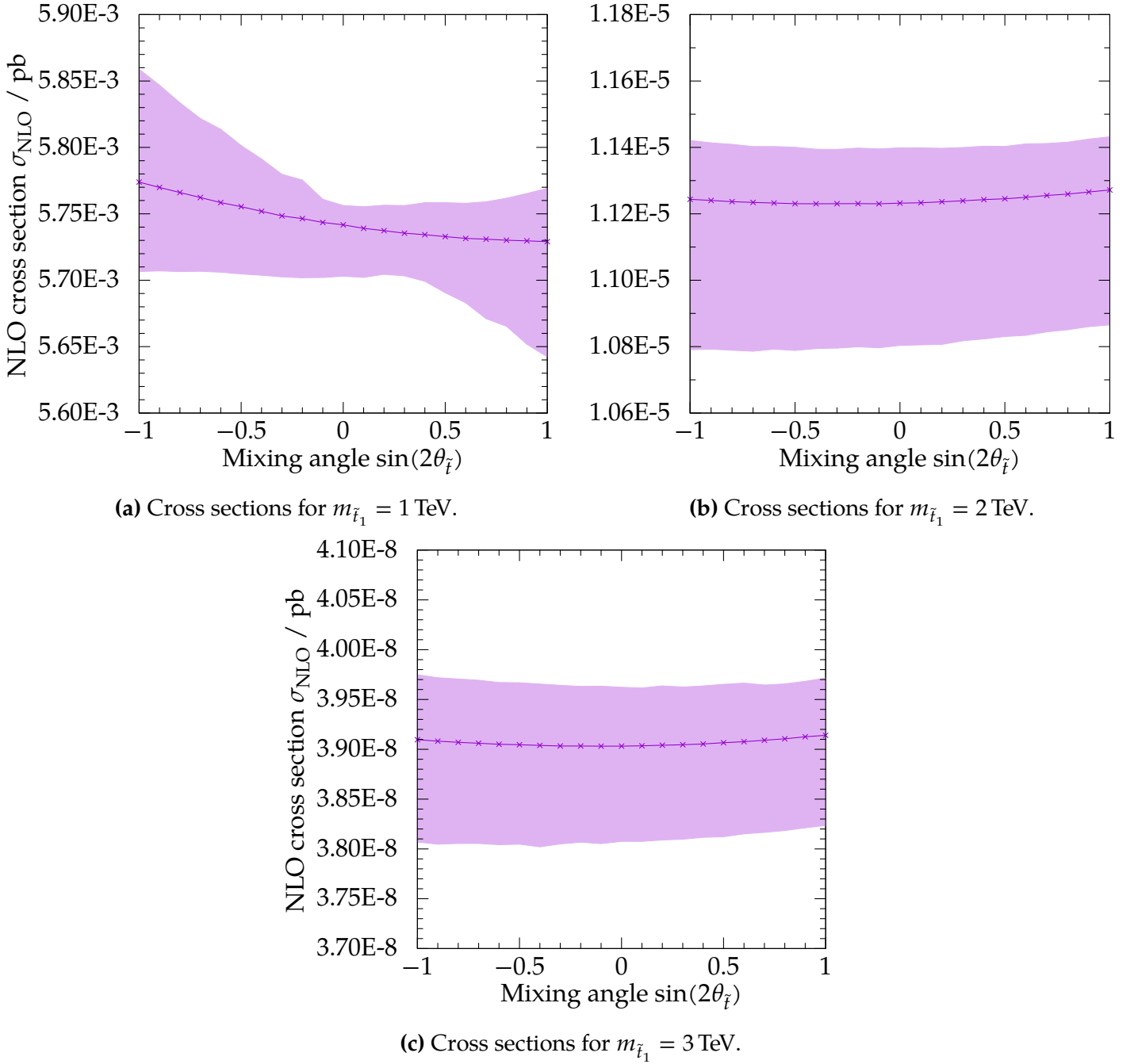


Figure 4.8.: NLO cross sections using Prospino, focusing on the parameter $\sin(2\theta_{\tilde{t}})$. The filled curve gives the variation of the cross section when independently varying $m_{\tilde{t}_2}$, $m_{\tilde{q}}$ and $m_{\tilde{g}}$ from 1 TeV to 10 TeV (step size 3 TeV), while the solid line represents the average over all data points.

5. Conclusion

The cross section for light stop pair-production for proton-proton collisions at $\sqrt{S} = 13$ TeV was calculated at leading order and next-to-leading order in this thesis. The dependence of the cross section on different parameters was analyzed. It was found to vary most strongly with the light stop mass $m_{\tilde{t}_1}$, as this parameter is already relevant at leading order.

The contributions by the other parameters – the heavy stop mass $m_{\tilde{t}_2}$, the light-flavor squark mass $m_{\tilde{q}}$, the gluino mass $m_{\tilde{g}}$ and the mixing angle $\sin(2\theta_{\tilde{t}})$ – were found to be much smaller, less than the contribution due to the NLO correction in general. The NLO cross section has been shown to vary in the percent range $\leq \pm 5\%$ from the average when varying these four parameters. Due to this, for leading-order and even (approximately) next-to-leading order treatments, it is possible to assume the cross section to be almost constant and independent of parameters other than $m_{\tilde{t}_1}$. At higher orders or if more accuracy is required, the parameter dependence becomes relevant. If the errors due to other sources are of the order 1%, the error in the cross section caused by the variation of the parameters presented here becomes significant and should be taken into account. The first parameter that should be taken into account is $m_{\tilde{g}}$, as it appeared to be the NLO parameter affecting the cross section most strongly. This is especially true around the singularity $m_{\tilde{t}_1} = m_{\tilde{g}} + m_t$, where the cross section varies strongly with $m_{\tilde{g}}$. The effect of the remaining parameters was weaker, with $m_{\tilde{q}}$ and $\sin(2\theta_{\tilde{t}})$ having intermediate effect and $m_{\tilde{t}_2}$ barely affecting the cross section at all.

The results can easily be extended to arbitrary collider energies \sqrt{S} (e. g. the LHC design energy $\sqrt{S} = 14$ TeV). Improvements on the accuracy could perhaps be achieved by incorporating the newer set of [MMHT14] PDFs into the NLO calculations as well. As all computations were executed on ordinary consumer hardware, it has become clear that for this five-parameter problem, even sampling the entire relevant parameter space is computationally feasible using appropriate equipment. For example, generating all data points where all five parameters assume 50 different values (corresponding to a granularity of 180 GeV steps in a 9 TeV range, for exam-

ple)¹ using 1000 CPU cores which can each generate data points at a rate of 1 s^{-1} , the computation would take about 3.6 days.

¹This is only for illustration – the parameters $m_{\bar{i}_1}$ and $m_{\bar{i}_2}$ have bounds restricting their range, requiring fewer data points, for example.

A. Notation and conventions

Throughout this work, the Einstein summation convention is employed unless noted otherwise. The signature of the metric tensor $g^{\mu\nu}$ is chosen to be $(+, -, -, -)$, i. e.

$$(g^{\mu\nu}) = (g_{\mu\nu}) = \begin{pmatrix} 1 & 0 & 0 & 0 \\ 0 & -1 & 0 & 0 \\ 0 & 0 & -1 & 0 \\ 0 & 0 & 0 & -1 \end{pmatrix}.$$

With this, the contravariant and covariant four-vectors are

$$(A^\mu) = (A^0, \vec{A}) \quad \text{and} \quad (A_\mu) = (A_0, -\vec{A}),$$

respectively. Accordingly, an inner product between two vectors x, y in Minkowski space is defined as

$$x \cdot y = x^\mu y_\mu = x^\mu g_{\mu\nu} y^\nu.$$

The so-called “Feynman slash notation” is used, which is given by

$$\not{A} = \gamma^\mu A_\mu$$

for any four-vector A , with the Dirac matrices γ^μ . Physical quantities are given in natural units, i. e. velocities are expressed in units of the speed of light in vacuum c and action or angular momenta are given in units of the reduced Planck constant \hbar . The notation employed is then

$$c = 1$$

$$\hbar = 1$$

with the physical dimension implicit in the seemingly dimensionless expressions on the right-hand side. The values for physical constants have been taken from [CODATA], unless noted otherwise. Commutators and anticommutators of two

operators A, B are denoted using

$$[A, B] = AB - BA \quad \text{and} \quad \{A, B\} = AB + BA$$

respectively. Where not stated otherwise, $\delta(x)$, $\theta(x)$ and δ_{ij} denote the Dirac δ distribution, the step function and the Kronecker symbol with the usual definitions.

In Feynman diagrams, time is taken to be increasing towards the right on the horizontal axis while space increases upwards on the vertical axis. Correspondingly, particles “travelling to the left” are antimatter particles. The usual conventions are followed: Fermions are represented by solid lines with arrows, scalar particles by dashed lines, gluons by curly lines and gluinos by curly lines with an additional solid line. Standard Model particles are labeled by their usual symbols, while the corresponding SUSY particles are endowed with a tilde. Anti-particles are denoted with a bar above. In calculations, the gauge was chosen such that $\xi = 1$, simplifying gluon propagators (cf. (2.22)). The strong coupling α_s is given by $\alpha_s = \frac{g_s^2}{4\pi}$.

B. Technical details

The version of Prospino used is Prospino1, which is publicly available at the address <http://tiger.web.psi.ch/proglist.html> [BHS96]. Prospino1 was modified to work with the [MSTW08] PDFs; this modified version was provided by Christoph Borschensky (borschensky@uni-muenster.de) in private communication. Numerical integrations were carried out using the VEGAS Monte Carlo integration algorithm [Lep78] implemented in the GNU Scientific Library (GSL), version 1.16 [Gal+]. Plots were created using gnuplot [W+14].

The calculations were performed using double-precision floating-point numbers. While rounding errors and accumulation of errors over many operations are always a concern in numerical computations, the amount of precision provided by 64 bit floating-point numbers should be more than sufficient compared to the numerical errors incurred due to the Monte Carlo integration. The errors estimates provided by VEGAS are assumed to be reliable. The fact that two independently written programs (although partially using the same library and data) provide exactly the same results also boosts confidence in the numerical computations.

I am grateful to Christoph Borschensky for many answers and explanations and to Prof. Kulesza for offering this subject as a bachelor's thesis.

Bibliography

- [AH13] Ian J. R. Aitchison and Anthony J. G. Hey. *Gauge Theories in Particle Physics*. Vol. 2: *Non-Abelian Gauge Theories: QCD and the Electroweak Theory*. 4th ed. CRC Press, 2013. ISBN: 978-1-4665-1310-5.
- [Ait05] Ian J. R. Aitchison. "Supersymmetry and the MSSM: An Elementary Introduction". 2005.
- [ATL14] The ATLAS, CDF, CMS, D0 Collaborations. *First combination of Tevatron and LHC measurements of the top-quark mass*. 2014. arXiv: 1403.4427v1 [hep-ex].
- [ATL15] ATLAS collaboration. *ATLAS Run 1 searches for direct pair production of third-generation squarks at the Large Hadron Collider*. 2015. arXiv: 1506.08616v1 [hep-ex].
- [Bee+10] Wim Beenakker et al. "Supersymmetric top and bottom squark production at hadron colliders". In: *JHEP* 1008:098 (2010). arXiv: 1006.4771v1 [hep-ph].
- [Bee+97] Wim Beenakker et al. "Squark and Gluino Production at Hadron Colliders". In: *Nucl. Phys. B* 492 (1997), pp. 51–103. arXiv: hep-ph/9610490v1.
- [Bee+98] Wim Beenakker et al. "Stop Production at Hadron Colliders". In: *Nucl. Phys. B* 515 (1998), pp. 3–14. arXiv: hep-ph/9710451v1.
- [BHS96] Wim Beenakker, R. Höpker, and M. Spira. *PROSPINO: A Program for the Production of Supersymmetric Particles in Next-to-leading Order QCD*. 1996. arXiv: hep-ph/9611232v1.
- [Bre11] Silja Breusing. "Resummation for supersymmetric particle production at hadron colliders". PhD thesis. RWTH Aachen, 2011. URL: <https://publications.rwth-aachen.de/record/82641>.

- [CODATA] P. J. Mohr, B. N. Taylor, and D. B. Newell. *The 2014 CODATA Recommended Values of the Fundamental Physical Constants. Web Version 7.0*. National Institute of Standards and Technology. 2015. URL: <http://physics.nist.gov/constants> (visited on 2015-09-18).
- [Cra14] Nathaniel Craig. *The State of Supersymmetry after Run I of the LHC*. 2014. arXiv: 1309.0528v2 [hep-ph].
- [Das08] Ashok Das. *Lectures on Quantum Field Theory*. World Scientific Publishing, 2008. ISBN: 978-981-283-285-6.
- [DGR04] Manuel Drees, Rohini M. Godbole, and Probir Roy. *Theory and Phenomenology of Sparticles. An account of four-dimensional $N = 1$ supersymmetry in High Energy Physics*. World Scientific Publishing, 2004. ISBN: 981-02-3739-1.
- [Fla92] Faye Flam. “The Quest for a Theory of Everything Hits Some Snags”. In: *Science* 256 (1992), pp. 1518–1519.
- [Gal+] M. Galassi et al. *GNU Scientific Library Reference Manual*. 3rd ed. ISBN: 0954612078. URL: <https://www.gnu.org/software/gsl>. GSL version 1.16.
- [Hab98] Howard E. Haber. “The Status of the Minimal Supersymmetric Standard Model and Beyond”. In: *Nucl. Phys. Proc. Suppl.* 62 (1998), pp. 469–484. arXiv: hep-ph/9709450v1.
- [HM84] Francis Halzen and Alan D. Martin. *Quarks and Leptons. The Fundamental Particles and Forces?* Wiley, 1984. ISBN: 0-471-88741-2.
- [Kan93] Gordon L. Kane. *Modern Elementary Particle Physics. The Fundamental Particles and Forces?* Addison-Wesley, 1993. ISBN: 0-201-62460-5.
- [Lep78] G. P. Lepage. “A New Algorithm for Adaptive Multidimensional Integration”. In: *J. Comput. Phys.* 27 (1978), pp. 192–203.
- [Mar11] Stephen P. Martin. *A Supersymmetry Primer*. 2011. arXiv: hep-ph/9709356v6.
- [Max14] Kevin Max. “Squark and Gluino production with non-degenerate masses at the LHC and future hadron colliders”. Bachelor’s thesis. Westfälische Wilhelms-Universität Münster, Aug. 11, 2014.
- [MMHT14] L. A. Harland-Lang et al. *Parton distributions in the LHC era: MMHT 2014 PDFs*. 2014. arXiv: 1412.3989v2 [hep-ph].

- [MSTW08] A. D. Martin et al. “Parton distributions for the LHC”. In: *Eur. Phys. J. C* 63 (2009), pp. 189–285. arXiv: 0901.0002v3 [hep-ph]. The PDF grids used for numerical calculations are modified versions of the publicly available grids; they were provided by Christoph Borschensky (borschensky@uni-muenster.de).
- [PS95] Michael E. Peskin and Daniel V. Schroeder. *Introduction to Quantum Field Theory*. Addison-Wesley, 1995. ISBN: 0-201-50397-2.
- [Ros09] Douglas Ross. *Lectures on Quantum Field Theory 1*. University of Southampton. 2009. URL: <https://www.southampton.ac.uk/~doug/ft1> (visited on 2015-09-18).
- [Sey05] Michael H. Seymour. *The Meaning of Feynman Diagrams*. CERN, 2005. URL: <https://indico.cern.ch/event/421552/session/21/material/0/0> (visited on 2015-09-22).
- [W+14] Thomas Williams, Colin Kelley, et al. *gnuplot 5.0.rc2*. Aug. 28, 2014. URL: <http://www.gnuplot.info>.

Erklärung

Hiermit versichere ich, dass ich die vorliegende Arbeit mit dem Titel „Properties of Supersymmetric Top Quark Pair-Production at Hadron Colliders“ selbständig verfasst habe, dass ich keine anderen Quellen und Hilfsmittel als die angegebenen benutzt habe und dass die Stellen der Arbeit, die anderen Werken – auch elektronischen Medien – dem Wortlaut oder Sinn nach entnommen wurden, auf jeden Fall unter Angabe der Quelle als Entlehnung kenntlich gemacht worden sind.

Münster, 30. September 2015

Ort, Datum

A handwritten signature in black ink, reading "Simon May". The signature is written in a cursive style with a horizontal line underneath it.

Unterschrift